

ACCURATE SIMULATIONS OF BINARY BLACK HOLE MERGERS IN FORCE-FREE ELECTRODYNAMICS

DANIELA ALIC¹, PHILIPP MOESTA^{1,2}, LUCIANO REZZOLLA^{1,3}, OLINDO ZANOTTI⁴, AND JOSÉ LUIS JARAMILLO¹

¹ Max-Planck-Institut für Gravitationsphysik, Albert-Einstein-Institut, Potsdam, Germany

² TAPIR, MC 350-17, California Institute of Technology, Pasadena, CA 91125, USA

³ Department of Physics and Astronomy, Louisiana State University, Baton Rouge, LA, USA

⁴ Laboratory of Applied Mathematics, University of Trento, Via Mesiano 77, 38123 Trento, Italy

Received 2012 April 7; accepted 2012 May 9; published 2012 July 3

ABSTRACT

We provide additional information on our recent study of the electromagnetic emission produced during the inspiral and merger of supermassive black holes when these are immersed in a force-free plasma threaded by a uniform magnetic field. As anticipated in a recent letter, our results show that although a dual-jet structure is present, the associated luminosity is ~ 100 times smaller than the total one, which is predominantly quadrupolar. Here we discuss the details of our implementation of the equations in which the force-free condition is not implemented at a discrete level, but rather obtained via a damping scheme which drives the solution to satisfy the correct condition. We show that this is important for a correct and accurate description of the current sheets that can develop in the course of the simulation. We also study in greater detail the three-dimensional charge distribution produced as a consequence of the inspiral and show that during the inspiral it possesses a complex but ordered structure which traces the motion of the two black holes. Finally, we provide quantitative estimates of the scaling of the electromagnetic emission with frequency, with the diffused part having a dependence that is the same as the gravitational-wave one and that scales as $L_{\text{EM}}^{\text{non-coll}} \approx \Omega^{10/3-8/3}$, while the collimated one scales as $L_{\text{EM}}^{\text{coll}} \approx \Omega^{5/3-6/3}$, thus with a steeper dependence than previously estimated. We discuss the impact of these results on the potential detectability of dual jets from supermassive black holes and the steps necessary for more accurate estimates.

Key words: binaries: close – galaxies: jets – gravitation – magnetic fields – plasmas – relativistic processes

Online-only material: color figures

1. INTRODUCTION

The gravitational interaction among galaxies, most of which are supposed to host a supermassive black hole (BH), with $M \geq 10^6 M_\odot$ (Shankar et al. 2004; Lou & Jiang 2008), is a well-established observational fact (Gopal-Krishna et al. 2003; Ellison et al. 2011; Mohamed & Reshetnikov 2011; Lambas et al. 2012). Moreover, in a few documented astrophysical cases, strong indications exist to believe that a binary merger among supermassive BHs has occurred or is ongoing (Rodriguez et al. 2006; Komossa et al. 2003; Dotti et al. 2009).

A strong motivation for studying supermassive binary black holes (SMBBHs) comes from the fact that their gravitational signal will be detected by the planned Laser Interferometric Space Antenna (eLISA/NGO; Amaro-Seoane et al. 2012; Binétruy et al. 2012). When combined with the usual electromagnetic (EM) emission, the detection of gravitational waves (GW) from these systems will provide a new tool for testing a number of fundamental astrophysical issues (Cornish & Porter 2007; Haiman et al. 2009; Phinney 2009). For this reason, SMBBHs are currently attracting widespread interest, both from an observational and a theoretical point of view (Rezzolla 2009; Reisswig et al. 2009; Kesden et al. 2010; Kocsis et al. 2011; Tanaka et al. 2012; Sesana et al. 2012; Barausse 2012). According to the simplest picture that has gradually emerged through a series of semi-analytical studies and numerical simulations (Milosavljeć & Phinney 2005; MacFadyen & Milosavljević 2008; Roedig et al. 2011; Bode et al. 2012), the accretion disk formed around the two merging BHs, commonly referred to as the “circumbinary” accretion disk, can follow the dynamical evolution of the system up until the dynamical timescale for the emission of GWs, which scales like $\sim D^4$, where D is the separation of the binary, be-

comes shorter than the viscous timescale, which instead scales like $\sim D^2$. When this happens, the circumbinary accretion disk is essentially decoupled from the binary, which rapidly enters the final stages of the inspiral. Under these conditions, neglecting the inertia of the accreting fluid can be regarded as a very good approximation. In contrast, magnetic fields generated by the circumbinary accretion disk could play an important role and the dynamics of the plasma in the inner region can then be described within the force-free (FF) approximation. These physical conditions are indeed similar to those considered in the seminal investigations of BH electrodynamics of Blandford and Znajek (Blandford & Znajek 1977), who addressed the question of whether the rotational energy of an isolated BH can be extracted efficiently by a magnetic field. After the first two-dimensional investigations of Komissarov and Barkov (Komissarov 2004; Komissarov & Barkov 2009), the numerical study of BH magnetospheres has now entered a mature phase in the context of SMBBHs evolution.

In an extensive analysis, but still in the absence of currents and charges, i.e., in electrovacuum, Mösta et al. (2010) showed that, even though the EM radiation in the lowest $\ell = 2$ and $m = 2$ multipole reflects the gravitational one, the energy emitted in EM waves is ~ 13 orders of magnitude smaller than that emitted in GWs for a reference binary with mass $M = 10^8 M_\odot$ and a magnetic field $B = 10^4$ G, thus casting serious doubts about a direct detection of the two different signals. However, a series of more recent numerical simulations in which currents and charges are taken into account have suggested the intriguing possibility that a mechanism similar to the original one proposed by Blandford and Znajek may be activated in the case of binaries (Palenzuela et al. 2009a, 2010a, 2010b, 2010c; Moesta et al. 2012; note that Palenzuela et al. 2010a, 2010b;

Moesta et al. 2012 also make use of an FF approximation). In particular, the Blandford–Znajek mechanism is likely to be valid under rather general conditions, namely even if stationarity and axisymmetry are relaxed and even if a non-spinning BH is simply boosted through a uniform magnetic field. Moreover, for such uniform magnetic field, the emitted EM flux shows a high degree of collimation, making the EM counterpart more easily detectable. A less optimistic view has emerged recently in Moesta et al. (2012, hereafter [Paper I](#)), where we have shown, through independent calculations in which the EM emission was extracted at much larger radii, that the dual-jet structure is indeed present but energetically subdominant with respect to the non-collimated and predominantly quadrupolar emission. In particular, even if the total luminosity at merger is ~ 100 times larger than in Palenzuela et al. (2010b), the energy flux is only ~ 8 – 2 times larger near the jets, thus yielding a collimated luminosity that is ~ 100 times smaller than the total one. As a result, [Paper I](#) indicated that the detection of the dual jets at the merger is difficult if not unlikely.

Here we provide additional information on the results presented in [Paper I](#) and discuss the details of our implementation of the equations in which the FF condition is obtained via a damping scheme which drives the solution to satisfy the correct condition. We show that this is important for a correct and accurate description of the current sheets that can develop in the course of the simulation. We also study in greater detail the three-dimensional charge distribution produced as a consequence of the inspiral and show that during the inspiral it has a complex structure tracing the motion of the two BHs. Finally, we provide quantitative estimates of the scaling of the EM emission with frequency, with the diffused part having a dependence that is the same as the GW one and that scales as $L_{\text{EM}}^{\text{non-coll}} \approx \Omega^{10/3-8/3}$, while the collimated one scales as $L_{\text{EM}}^{\text{coll}} \approx \Omega^{5/3-6/3}$, thus with a steeper dependence than previously estimated by Palenzuela et al. (2010b).

This paper is organized as follows. In Section 2 we describe the system of equations considered in our analysis, with particular emphasis on the treatment of the FF condition, while in Section 3 we discuss the different routes to the calculation of the EM radiated quantities. In Section 4 we present the astrophysical setup of a BH binary merger, while Section 5 compares different approaches for the enforcement of the FF condition. Section 6 is devoted to the presentation of the results, and, in particular, to the computation of the luminosity. Finally, Section 7 presents the conclusion of our work and the prospects for the detection of an EM counterpart to SMBBHs.

In the rest of the paper, we set $c = G = 1$, adopt the standard convention for the summation over repeated indices with Greek indices running from 0 to 3, Latin indices from 1 to 3, and make use of the Lorentz–Heaviside notation for the EM quantities, in which all $\sqrt{4\pi}$ factors disappear.

2. EVOLUTION EQUATIONS

We solve the combined system defined by the Einstein and Maxwell equations and model either an isolated rotating BH or a BH binary inspiralling in quasi-circular orbits. In both cases we assume that there is an external FF magnetic field. More specifically, we solve the Einstein equations

$$R_{\mu\nu} - \frac{1}{2}Rg_{\mu\nu} = 8\pi T_{\mu\nu}, \quad (1)$$

where $R_{\mu\nu}$, $g_{\mu\nu}$, and $T_{\mu\nu}$ are the Ricci, the metric, and the stress-energy tensors, respectively. In addition, we solve the following extended set of Maxwell equations (Komissarov 2007; Palenzuela et al. 2009b):

$$\nabla_\mu (F^{\mu\nu} + g^{\mu\nu}\Psi) = I^\nu - \kappa n^\nu \Psi, \quad (2)$$

$$\nabla_\mu (*F^{\mu\nu} + g^{\mu\nu}\Phi) = -\kappa n^\nu \Phi, \quad (3)$$

where $F_{\mu\nu}$ is the Faraday tensor, $*F_{\mu\nu}$ is its dual, I^μ is the four-current, and we have introduced a 3+1 slicing of spacetime, with n^μ being the unit (future oriented) timelike vector associated with a generic normal observer to the spatial hypersurfaces.

The set of Maxwell Equations (2) and (3) is referred to as “extended” because it incorporates the so-called divergence-cleaning approach, originally presented in Dedner et al. (2002) in flat spacetime, and which amounts to introducing two additional scalar fields, Ψ and Φ , that propagate away the deviations of the divergences of the electric and of the magnetic fields from the values prescribed by Maxwell equations. Such scalar fields are initialized to zero, but are driven into evolution as soon as violations of the EM constraints are produced. The total stress-energy tensor is composed of a term corresponding to the EM field:

$$T_f^{\mu\nu} \equiv F^\mu{}_\lambda F^{\nu\lambda} - \frac{1}{4}(F^\lambda{}_\kappa F_{\lambda\kappa})g^{\mu\nu}, \quad (4)$$

and of a term due to matter, $T_m^{\mu\nu}$. However, because the EM field is assumed to be FF, $T_f^{\mu\nu} \gg T_m^{\mu\nu}$, and the total stress-energy tensor is then assumed to be given entirely by Equation (4), namely $T^{\mu\nu} \approx T_f^{\mu\nu}$. In the rest of our discussion we will use the expression “electrovacuum” to denote the case when currents and charges of the Maxwell equations are zero. Such a scenario was extensively studied in Mösta et al. (2010) and it will be used here as an important reference. In the following we discuss in more detail our strategy for the solution of the Einstein equations and of the Maxwell system in an FF regime.

2.1. The Einstein Equations

For the solution of the Einstein equations we make use of a three-dimensional finite-differencing code that adopts a conformal-traceless “3 + 1” BSSNOK formulation of the equations (see Pollney et al. 2007 for the full expressions in vacuum and Baiotti et al. 2008 for the case of a spacetime with matter). The code is based on the Cactus Computational Toolkit (Allen et al. 2000) and employs adaptive mesh-refinement techniques via the Carpet-driver (Schnetter et al. 2004). For compactness we will not report here the details regarding the adopted formulation of the Einstein equations and the gauge conditions used, which can, however, be found in Pollney et al. (2007, 2011).

We also note that recent developments, such as the use of eighth-order finite-difference operators or the adoption of a multiblock structure to extend the size of the wave zone, have been recently presented in Pollney et al. (2009, 2011). Here, however, in order to limit the computational costs and because a very high accuracy in the waveforms is not needed, the multiblock structure was not used and we have used a fourth-order finite-difference operator with a third-order Implicit-Explicit Runge–Kutta (RKIMEX) integration in time (see Section 2.3).

2.2. The Maxwell Equations

The Maxwell Equations (2) and (3) take a more familiar form when expressed in terms of the standard electric and magnetic fields as defined by the following decomposition of the Faraday tensor in a 3+1 foliation:

$$F^{\mu\nu} = n^\mu E^\nu - n^\nu E^\mu + \epsilon^{\mu\nu\alpha\beta} B_\alpha n_\beta, \quad (5)$$

$${}^*F^{\mu\nu} = n^\mu B^\nu - n^\nu B^\mu - \epsilon^{\mu\nu\alpha\beta} E_\alpha n_\beta, \quad (6)$$

where the vectors E^μ and B^μ are purely spatial (i.e., $E^\mu n_\mu = B^\mu n_\mu = 0$) and correspond to the electric and magnetic fields measured by the normal (Eulerian) observers. The two extra scalar fields Ψ and Φ introduced in the extended set of Maxwell equations lead to two evolution equations for the EM constraints, which, we recall, are given by the divergence equations

$$\nabla_i E^i = q, \quad (7)$$

$$\nabla_i B^i = 0, \quad (8)$$

where the electric current has been decomposed in the electric charge density $q \equiv -n_\mu I^\mu$ and the spatial current $J_i \equiv I_i$. More specifically, these evolution equations describe damped wave equations and have the effect of dynamically controlling the possible growth of the violations of the constraints and of propagating them away from the problematic regions of the computational domain where they are produced.

In terms of E^μ and B^μ , the 3+1 formulation of Equations (2) and (3) becomes (Palenzuela et al. 2010a)

$$\mathcal{D}_t E^i - \epsilon^{ijk} \nabla_j (\alpha B_k) + \alpha \gamma^{ij} \nabla_j \Psi = \alpha K E^i - \alpha J^i, \quad (9)$$

$$\mathcal{D}_t B^i + \epsilon^{ijk} \nabla_j (\alpha E_k) + \alpha \gamma^{ij} \nabla_j \Phi = \alpha K B^i, \quad (10)$$

$$\mathcal{D}_t \Psi + \alpha \nabla_i E^i = \alpha q - \alpha \kappa \Psi, \quad (11)$$

$$\mathcal{D}_t \Phi + \alpha \nabla_i B^i = -\alpha \kappa \Phi, \quad (12)$$

$$\mathcal{D}_t q + \nabla_i (\alpha J^i) = \alpha K q, \quad (13)$$

where $\mathcal{D}_t \equiv (\partial_t - \mathcal{L}_\beta)$ and \mathcal{L}_β is the Lie derivative along the shift vector β and K is the trace of the extrinsic curvature. The charge density q can be computed either through the evolution (Equation (13)) or by inverting the constraint (Equation (7)). For simplicity, we choose the latter approach, which ensures that the constraint (12) is automatically satisfied if $\Psi = 0$ initially and effectively removes the need for the potential Ψ .

Exploiting now that the covariant derivative in the second term of Equations (10) and (11) reduces to a partial derivative, i.e.,

$$\epsilon^{ijk} \nabla_j B_k = \epsilon^{ijk} (\partial_j B_k + \Gamma_{jk}^l B_l) = \epsilon^{ijk} \partial_j B_k, \quad (14)$$

and using a standard conformal decomposition of the spatial 3-metric

$$\tilde{\gamma}_{ij} = e^{4\phi} \gamma_{ij}, \quad \phi = \frac{1}{12} \ln \gamma, \quad (15)$$

we obtain the final expressions for the extended Maxwell equations that we actually evolve

$$\begin{aligned} \mathcal{D}_t E^i - \epsilon^{ijk} e^{4\phi} [(\partial_j \alpha) \tilde{\gamma}_{ck} B^c + \alpha (4 \tilde{\gamma}_{ck} \partial_j \phi + \partial_j \tilde{\gamma}_{ck}) B^c \\ + \alpha \tilde{\gamma}_{ck} \partial_j B^c] = \alpha K E^i - \alpha J^i, \end{aligned} \quad (16)$$

$$\begin{aligned} \mathcal{D}_t B^i + \epsilon^{ijk} e^{4\phi} [(\partial_j \alpha) \tilde{\gamma}_{ck} E^c + \alpha (4 \tilde{\gamma}_{ck} \partial_j \phi + \partial_j \tilde{\gamma}_{ck}) E^c \\ + \alpha \tilde{\gamma}_{ck} \partial_j E^c] + \alpha e^{-4\phi} \tilde{\gamma}^{ij} \nabla_j \Phi = \alpha K B^i, \end{aligned} \quad (17)$$

$$\mathcal{D}_t \Phi + \alpha \nabla_i B^i = -\alpha \kappa \Phi. \quad (18)$$

Clearly, the standard Maxwell equations in a curved background are recovered for $\Phi = 0$, so that the Φ scalar can then be considered as the normal-time integral of the standard divergence constraint (8), which propagates at the speed of light and is damped during the evolution.

As mentioned above, the coupling of the Einstein to the Maxwell equations takes place via the inclusion of a nonzero stress-energy tensor for the EM fields which is built in terms of the Faraday tensor as dictated by Equation (4). More specifically, the relevant components of the stress-energy tensor can be obtained in terms of the electric and magnetic fields, that is as

$$\tau \equiv n_\mu n_\nu T^{\mu\nu} = \frac{1}{8\pi} (E^2 + B^2), \quad (19)$$

$$S_i \equiv -n_\mu T^\mu_i = \frac{1}{4\pi} \epsilon_{ijk} E^j B^k, \quad (20)$$

$$S_{ij} \equiv T_{ij} = \frac{1}{4\pi} \left[-E_i E_j - B_i B_j + \frac{1}{2} \gamma_{ij} (E^2 + B^2) \right], \quad (21)$$

where $E^2 \equiv E^k E_k$ and $B^2 \equiv B^k B_k$. The scalar function τ can be identified with the energy density of the EM field, while the energy flux S_i is the Poynting vector.

As already discussed in the Introduction, we remark again that the EM energies that will be considered here are so small when compared with the gravitational binding ones that the contributions of the stress-energy tensor to the right-hand side of the Einstein Equations (1) are effectively negligible and thus can be set to zero, reducing the computational costs. The fully coupled set of the Einstein–Maxwell equations was considered in Palenzuela et al. (2009a, 2010c) and the comparison with the results obtained here suggests that for the fields below $\lesssim 10^8$ G, the use of the test-field approximation is fully justified.

2.3. Numerical Treatment of the Force-free Conditions

As noted before, within an FF approximation the stress-energy tensor is dominated by the EM part and the contribution coming from the matter can be considered zero. Following Palenzuela et al. (2010a), the conservation of energy and momentum, $\nabla_\nu T^{\mu\nu} = 0$, implies that also the Lorentz force is negligible, i.e.,

$$0 = \nabla_\nu T^{\mu\nu} \approx \nabla_\nu T_f^{\mu\nu} = -F^{\mu\nu} I_\nu, \quad (22)$$

which can also be written equivalently in terms of quantities measured by Eulerian observers as

$$E^k J_k = 0, \quad (23)$$

$$qE^i + \epsilon^{ijk} J_j B_k = 0. \quad (24)$$

Computing the scalar and vector product of the equations above with the magnetic field B^i , we obtain

$$E^k B_k = 0, \quad (25)$$

$$J^i = q \frac{\epsilon^{ijk} E_j B_k}{B^2} + J_B \frac{B^i}{B^2}. \quad (26)$$

The first relation (25) implies that the electric and magnetic fields are orthogonal, while expression (26) defines the current, whose component parallel to the magnetic field, namely $J_B \equiv J^i B_i$, needs to be defined via a suitable Ohm law. From the numerical point of view, specific strategies must be adopted in order to enforce the FF constraints expressed by Equations (25) and (26). In fact, even though such constraints are exactly satisfied at time $t = 0$, there is no guarantee that they will remain so during the evolution of the system.

The approach introduced by Palenzuela et al. (2010a) to enforce the constraints (25) and (26) consists in a modification of the system at the discrete level, by redefining the electric field after each timestep in order to remove any component parallel to the magnetic field. In other words, after each timestep the newly computed electric field is “cleaned” by imposing the following transformation (Palenzuela et al. 2010a)

$$E^i \rightarrow E^i - (E^k B_k) \frac{B^i}{B^2}. \quad (27)$$

In addition, the current is computed from Equation (26) after setting $J_B = 0$. An alternative approach, introduced in Komissarov (2011) and then in Lyutikov (2011), uses the Maxwell equations to compute $\mathcal{D}_t(E^k B_k)$, which has to vanish according to Equation (25). Using Equations (10) and (11) it is then easy to obtain the following prescription for J_B :

$$J_B = \frac{1}{\alpha} [B_i \epsilon^{ijk} \nabla_j (\alpha B_k) - E_i \epsilon^{ijk} \nabla_j (\alpha E_k)]. \quad (28)$$

Without further modifications, however, this approach leads to large violations of the FF constraint (25) in long-term numerical simulations, as it does not provide a mechanism for imposing the constraint at later times.

As we will show later on, both approaches (27) and (28) are not fully satisfactory and, as a consequence, here we present an alternative method, which takes inspiration from the treatment of currents (and related stiff source terms) in resistive magnetohydrodynamics. The idea of introducing a suitable Ohm law was proposed in Komissarov (2004) and then in Palenzuela et al. (2010a), but it has not been used so far in numerical simulations, due to the presence of stiff terms which appear as a result. In practice, our continuum approach is equivalent to the insertion of suitable driver terms, so that the parallel component J_B is computed from an Ohm law of the type

$$J_B = \sigma_B E^k B_k, \quad (29)$$

where σ_B is the anisotropic conductivity along the magnetic-field lines. This additional term in the current acts like a damping term in the evolution $\partial_t(E^k B_k)$, and enforces the constraint (25) on a timescale $1/\sigma_B$. For σ_B sufficiently large, one can ensure that the FF constraint (25) is always satisfied. In the simulations

presented in this paper, we choose $\sigma_B > 1/\Delta t$, where Δt is the timestep on the finest refinement level. The resulting hyperbolic system with stiff terms is solved using a third-order RKIMEX time integration method with the technical implementation following the one discussed in Palenzuela et al. (2009b) and with additional details presented in the Appendix.

An additional problem in the numerical treatment of the FF approach is represented by the development of current sheets, namely of regions where the electric field becomes larger than the magnetic field, such that the condition

$$B^2 - E^2 > 0 \quad (30)$$

is violated. If this happens, and in the absence of a proper Ohm law responsible for the resistive effects, the Alfvén wave speed becomes complex and the system of FF equations is no longer hyperbolic (Komissarov 2004). Under realistic conditions, one expects that in these regions an anomalous and isotropic resistivity would restore the dominance of the magnetic field. A solution to this problem was proposed in Komissarov (2006), where the velocity of the drift current was modified in order to ensure that it is always smaller than the speed of light. This leads to the following prescription for the current:

$$J^i = q \frac{\epsilon^{ijk} E_j B_k}{B^2 + E^2} + J_B \frac{B^i}{B^2}, \quad (31)$$

which should be compared with Equation (26) and has the net result of underestimating the value of the current.

An alternative solution to the numerical treatment of current sheets consists in a modification of the system again at the discrete level (Palenzuela et al. 2010a). In practice, after each timestep a correction is applied “by hand” to the magnitude of the electric field in order to keep it smaller than the magnetic field, i.e.,

$$E^i \rightarrow E^i \left[(1 - \Theta) + \Theta \sqrt{\frac{B^2}{E^2}} \right], \quad (32)$$

with $\Theta = 1$ when $B^2 - E^2 < 0$ and $\Theta = 0$ otherwise.

Our strategy, however, differs from both the previous ones and follows the same philosophy behind the choice of the driver defined by Equation (29). We therefore introduce a second driver in Ohm law, which will act as a damping term for the electric field in those cases when $E^2 > B^2$. This additional term, combined with the prescription for the parallel part of the current (29), leads to the following effective Ohm law:

$$J^i = q \frac{\epsilon^{ijk} E_j B_k}{B^2} + \sigma_B (E^k B_k) \frac{B^i}{B^2} - \sigma_B (B^2 - E^2) E^i \frac{E^2}{B^2}. \quad (33)$$

Expression (33) shows therefore that in normal conditions, i.e., when $B^2 - E^2 \gtrsim 0$, the last term introduces a very small and negative current along the direction of the electric field. However, should a violation of the condition (30) take place, a positive current is introduced, which reduces the strength of the electric field and restores the magnetic dominance.

In Section 5 we will compare the different prescriptions for the enforcement of the FF condition and show that, in contrast to recipes (27) and (32), our suggestions (29) and (33) yield both accurate and a smooth distribution of the EM currents.

3. ANALYSIS OF RADIATED QUANTITIES

The calculation of the EM and gravitational radiation generated during the inspiral, merger, and ringdown is an important aspect of this work as it allows us to measure the amount correlation between the two forms of radiation. We compute the gravitational radiation via the Newman-Penrose curvature scalars. In practice, we define an orthonormal basis in the three-dimensional space $(\hat{r}, \hat{\theta}, \hat{\phi})$, with poles along \hat{z} . Using the normal to the slice as timelike vector \hat{t} , we construct the null orthonormal tetrad $\{l, n, m, \bar{m}\}$:

$$l = \frac{1}{\sqrt{2}}(\hat{t} + \hat{r}), \quad n = \frac{1}{\sqrt{2}}(\hat{t} - \hat{r}), \quad m = \frac{1}{\sqrt{2}}(\hat{\theta} + i\hat{\phi}), \quad (34)$$

with the bar indicating a complex conjugate. Adopting this tetrad, we project the Weyl curvature tensor $C_{\alpha\beta\gamma\delta}$ to obtain $\Psi_4 \equiv C_{\alpha\beta\gamma\delta} n^\alpha \bar{m}^\beta n^\gamma \bar{m}^\delta$, that measures, ideally at null infinity, the outgoing gravitational radiation. For the EM emission, on the other hand, we use two equivalent approaches to cross-validate our measures. The first one uses the Newman-Penrose scalars Φ_0 (for the ingoing EM radiation) and Φ_2 (for the outgoing EM radiation), defined using the same tetrad (Teukolsky 1973):

$$\Phi_0 \equiv F^{\mu\nu} l_\nu m_\mu, \quad \Phi_2 \equiv F^{\mu\nu} \bar{m}_\nu n_\mu. \quad (35)$$

By construction, the Newman-Penrose scalars Ψ_4, Φ_0, Φ_2 are dependent on the null tetrad (34), so that truly unambiguous scalars are measured only at very large distances from the sources, where inertial observers provide preferred choices. Any measure of these quantities in the strong-field region is therefore subject to ambiguity and risks producing misleading results. As an example, the EM energy flux does not show the expected $1/r^2$ scaling when Φ_2 and Φ_0 are measured at distances of $r \simeq 20M$, as used in Palenzuela et al. (2010a, 2010b), which is instead reached only for $r \gtrsim 100M$. As we will show in Section 6, this fact is responsible for significant differences in the estimates of the non-collimated EM emission.

The use of a uniform magnetic field within the computational domain has a number of drawbacks, most notably, nonzero initial values of Φ_2, Φ_0 . As a result, great care has to be taken when measuring the EM radiation. Fortunately, we can exploit the linearity in the Maxwell equations to distinguish the genuine emission induced by the presence of the BH(s) from the background one. Following Teukolsky (1973), we compute the total EM luminosity as a surface integral across a 2-sphere at a large distance:

$$L_{\text{EM}} = \lim_{r \rightarrow \infty} \frac{1}{2\pi} \int r^2 (|\Phi_2|^2 - |\Phi_0|^2) d\Omega, \quad (36)$$

which results straightforwardly from the integration of the component of EM stress-energy tensor (4) along the timelike vector n^μ and the normal direction to the large 2-sphere (namely, the flux of the Poynting vector in Equation (19) through the 2-sphere). The term Φ_0 in Equation (36) has been maintained (it disappears at null infinity) to account for the possible presence of an ingoing component in the radiation at finite distances. In particular, Equation (36) shows that the net flux is obtained by adding (with the appropriate sign) the respective contributions of the outgoing and ingoing fluxes. More specifically, in terms of the complex scalars Φ_2 and Φ_0 , the outgoing net flux is obtained by subtracting the square of their respective moduli. In the specific scenario considered here,

where a nonzero non-radiative component of the magnetic field extends to large distances, expression (36) must be modified. More specifically we rewrite it as

$$L_{\text{EM}} = \lim_{r \rightarrow \infty} \frac{1}{2\pi} \int r^2 (|\Phi_2 - \Phi_{2,B}|^2 - |\Phi_0 - \Phi_{0,B}|^2) d\Omega, \quad (37)$$

where $\Phi_{2,B}$ and $\Phi_{0,B}$ are the values of the background scalars induced by the asymptotically uniform magnetic-field solution in the time-dependent spacetime produced by the binary BHs. Under the assumption of a vanishing net ingoing radiation, i.e., $\Phi_0 \approx \Phi_{0,B}$ and of stationarity of the background field, i.e., $\Phi_{2,B} \approx \Phi_{0,B}$, expression (37) can also be rewritten as (Neilsen et al. 2011; Ruiz et al. 2012)

$$L_{\text{EM}} = \lim_{r \rightarrow \infty} \frac{1}{2\pi} \int r^2 (|\Phi_2 - \Phi_0|^2) d\Omega. \quad (38)$$

Although Equation (38) does not represent, at least in a strict physical and mathematical sense, a valid expression for the emission of EM radiation in generic scenarios, it can provide a useful recipe whenever the assumed approximations made above are actually fulfilled. In Section 6 we will assess to what degree this is the case for the specific scenario and model considered here.

The choice of the background values of the Newman-Penrose scalars $\Phi_{2,B}$ and $\Phi_{0,B}$ plays a crucial role in measuring correctly the radiative EM emission, since these quantities are themselves time dependent and cannot be distinguished, at least a priori, from the purely radiative contributions. This introduces an ambiguity in the definition of $\Phi_{2,B}$ and $\Phi_{0,B}$, which can, however, be addressed in at least two different ways. The first one consists in assuming that the background values are given by the initial values, and further neglecting their time dependence, namely setting

$$\Phi_{2,B} = \Phi_2(t=0), \quad \Phi_{0,B} = \Phi_0(t=0). \quad (39)$$

Since all the $m=0$ multipoles of the Newman-Penrose scalars are not radiative, a second way to resolve the ambiguity is to remove those multipole components from the estimates of the scalars, namely, of defining

$$\Phi_{2,B} = (\Phi_2)_{\ell,m=0}, \quad \Phi_{0,B} = (\Phi_0)_{\ell,m=0}, \quad (40)$$

where $(\Phi_2)_{\ell,m=0}$ refer to the $m=0$ modes of the multipolar decomposition of Φ_2 ($\ell \leq 8$ is sufficient to capture most of the background). Note also that because the $m=0$ background is essentially time independent (after the initial transient), the choice (40) is effectively equivalent to the assumption that the background is given by the final values of the Newman-Penrose scalars as computed in an electrovacuum evolution of the same binary system. While apparently different, expressions (39) and (40) lead to very similar estimates (see Section 6.1) and, more importantly, they have a simple interpretation in terms of the corresponding measures that they allow.

The second approach that we have followed for the computation of the emitted luminosity is the evaluation of the flux of the Poynting vector across a 2-sphere at large distances in terms of the more familiar 3+1 fields E^i and B^i in Equation (19). Of course, such evaluation is adequate only far from the binary. The purpose of implementing both versions of the luminosity calculation, which are conceptually equivalent but differ in the technical details, is precisely to quantify the error introduced by

evaluating the flux at large but finite distances via the Newman-Penrose scalars Φ_2 and Φ_0 . Also in this case, to account for the background non-radiative contribution due to our choice of uniform magnetic field (and using again the linearity in the Maxwell equations), we need to remove the background values of the EM fields E_B^j , B_B^j . The relevant part of the Poynting vector is then computed as

$$S_i = \sqrt{\gamma} \epsilon_{ijk} (E^j - E_B^j) (B^k - B_B^k), \quad (41)$$

where, consistently with expression (39), we set

$$E_B^k = E^k(t=0) = 0, \quad B_B^k = B^k(t=0) \neq 0. \quad (42)$$

As we will show in Sections 6.2 and 6.1, we have verified that the measures of the EM luminosity obtained using Equation (39) or Equation (40) reproduces well the corresponding ones obtained using the Poynting vector in Equation (41).

4. ASTROPHYSICAL SETUP AND INITIAL DATA

As mentioned in the Introduction, the astrophysical scenario we have in mind is represented by the merger of supermassive BH binaries resulting from galaxy mergers. More specifically, we consider the astrophysical conditions during and after the merger of two supermassive BHs, each of which is surrounded by an accretion disk. As the merger between the two galaxies takes place and the BHs get closer, a single “circumbinary” accretion disk is expected to form, reaching a stationary accretion phase. During this phase, the binary evolves on the dynamical viscous timescale τ_d of the circumbinary accretion disk, which is regulated by the ability of the disk to transport its angular momentum outward (either via shear viscosity or magnetically mediated instabilities). On a much longer radiation-reaction timescale τ_{GW} , the system loses both energy and angular momentum through the emission of GWs, hence progressively reducing the binary separation D . As a consequence, for most of the evolution the disk slowly follows the binary as its orbit shrinks. However, because τ_{GW} and τ_d have a very different scaling with D , more specifically, $\tau_{\text{GW}} \sim D^4$, while $\tau_d \sim D^2$, at a certain time the timescale τ_{GW} becomes smaller than τ_d . When this happens, the disk becomes disconnected from the binary, the mass accretion rate reduces substantially and the binary performs its final orbits in an “interior” region which is essentially devoid of gas (Armitage & Natarajan 2002; Liu et al. 2003; Milosavljeć & Phinney 2005). This represents the astrophysical scenario in which our simple model is then built.

Although poor in gas, the inner region is coupled to the circumbinary disk via a large-scale magnetic field, which we assume to be anchored to the disk. The inner edge of the disk is at a distance of $\sim 10^3 M$ and is effectively outside of our computational domain, while the binary separation is only of $D \sim 10 M$. For simplicity, and because a large-scale dipolar field will appear as essentially uniform on the orbital length scale of the binary during the final stages of the inspiral, we use an initially uniform magnetic within the computational domain. More specifically, the initial magnetic field has Cartesian components given simply by $B^i = (0, 0, B_0)$ with $B_0 M = 10^{-4}$ in geometric units or $B_0 \sim 10^8 \text{ G}$ for a binary with total mass $M = 10^8 M_\odot$.⁵ Furthermore, because

we consider the initial conditions to represent a tenuous plasma electrically neutral, the charges, electric currents, and the initial electric field are all assumed to be zero, i.e., $E^i = 0 = q$.

We note that although reasonable, the assumption of a large-scale uniform magnetic field has a deep impact on the results obtained and more realistic magnetic-field topologies will be considered in our future work. As mentioned earlier, although astrophysically large, the initial magnetic field considered here has an associated EM energy which is several orders of magnitude smaller than the gravitational-field energy and can be treated as a test field. On the other hand, the combination of very low densities and strong magnetic fields makes the FF approximation rather appropriate for capturing the dynamics of the tenuous plasma.

4.1. Initial Data and Grid Setup

We construct consistent BH initial data via the “puncture” method as described in Ansorg et al. (2004). We consider binaries with equal masses but with two different spin configurations: namely, the s_0 binary, in which both BHs are non-spinning, and the s_6 binary, in which both BHs have spins aligned with the orbital angular momentum. We use these two configurations to best isolate the effects due to the binary orbital motion from those related to the spins of the two BHs.

We note that similar initial data were considered by Koppitz et al. (2007), Pollney et al. (2007), and Rezzolla et al. (2008a, 2008b, 2008c) but we have recalculated them here using a higher resolution and improved initial orbital parameters. More specifically, we use post-Newtonian (PN) evolutions following the scheme outlined in Husa et al. (2008), which provides a straightforward prescription for initial-data parameters with small initial eccentricity, and which can be interpreted as part of the process of matching our numerical calculations to the inspiral described by the PN approximations. The free parameters of the puncture initial data are then (1) the puncture coordinate locations, (2) the puncture bare mass parameters, (3) the linear momenta, and (4) the individual spins. The parameters of the models adopted in the numerical simulations can be found in Koppitz et al. (2007), Pollney et al. (2007), and Rezzolla et al. (2008a, 2008b, 2008c). In brief, the initial separation is $D = 8 M$ for all of them, where M is the total initial BH mass,⁶ chosen as $M = 1$, while the individual asymptotic initial BH masses are $M_i = 1/2$. In addition, the EM field is initialized to $B^i = (0, 0, B_0)$ with $B_0 \sim 10^{-4}/M \sim 10^8 (10^8 M_\odot/M) \text{ G}$ and $E^i = 0$.

The numerical grids consist of nine levels of mesh refinement, with a fine-grid resolution of $\Delta x/M = 0.025$. The wave-zone grid, in which our wave extraction is carried out, has a resolution of $\Delta x/M = 1.6$, and extends from $r = 24 M$ to $r = 180 M$. Finally, the outer (coarsest) grid extends up to a distance of $\sim 820 M$ in each coordinate direction. Shorter, higher-resolution simulations have also been carried out to perform consistency checks. Finally, in addition to BHs in a binary system, we have also considered spinning and non-spinning isolated BHs as testbeds for our implementation of the FF condition. In this case, the numerical grids consist of seven levels of mesh refinement, with a fine-grid resolution of $\Delta x/M = 0.04$ and a coarse-grid resolution of $\Delta x/M = 2.56$, placing the outer boundary at a distance of $\sim 410 M$ in each coordinate direction.

⁵ Smaller values of the magnetic field would lead to a less accurate estimates of the EM fields, but have also been considered. No appreciable differences have been measured when using a magnetic field $B_0 M = 10^{-6}$.

⁶ Note that the initial Arnowitt, Deser, Misner (ADM) mass of the spacetime is not exactly 1 due to the binding energy of the BHs.

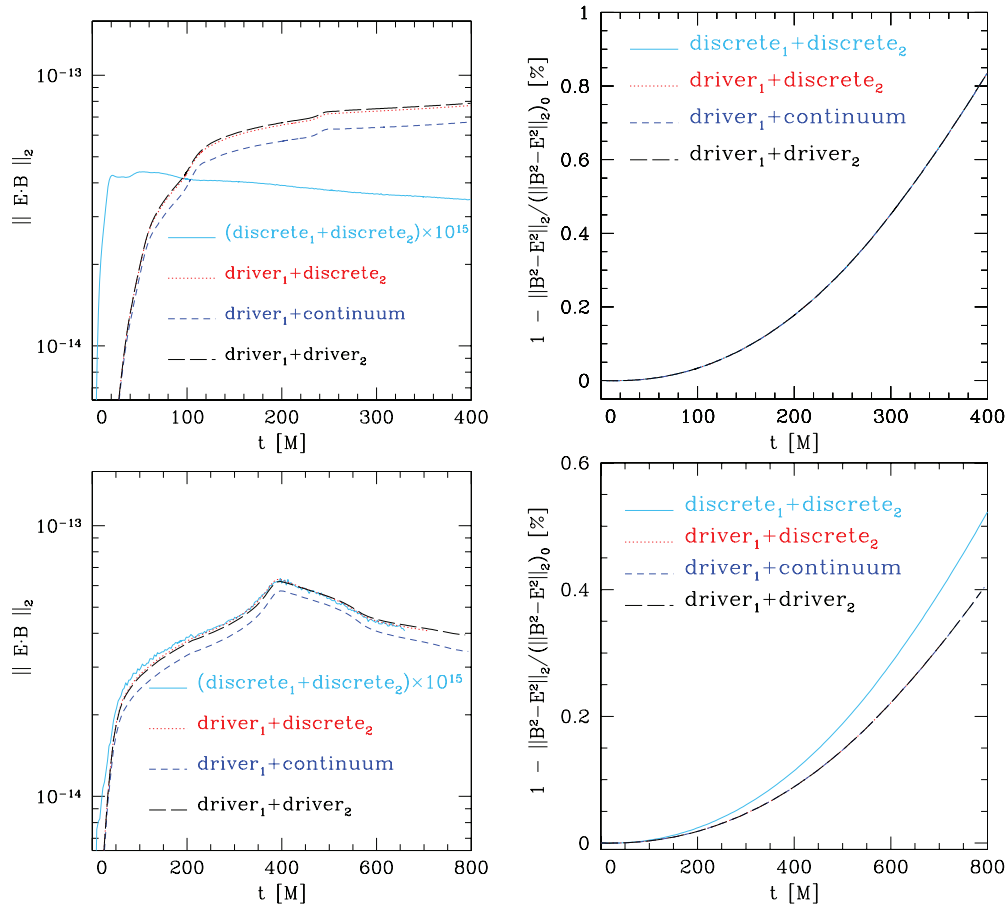


Figure 1. Top row: orthogonality condition (left panel) and current-sheet condition (right panel) for a single spinning BH (dimensionless spin parameter $a = J/M^2 = 0.7$), using different prescriptions for the current: fully discrete approach (light-blue solid line), driver₁ plus discrete₂ (red dotted line), driver₁ plus continuum (dark-blue dashed line), driver₁ plus driver₂ (black long-dashed line). Bottom row: the same as in the top row, but for the equal-mass non-spinning binary BH system s_0 .

(A color version of this figure is available in the online journal.)

5. ACCURATE FORCE-FREE ENFORCEMENT

As mentioned in Section 2.3, several different approaches are possible to enforce the FF conditions (25) and (26) in the plasma. The important advantage of the discretized approach introduced by Palenzuela et al. (2010a) is that, at least globally, it gives the desired result of an FF solution. In fact, since this approach acts “by hand” on the EM fields and converts them to values which would yield an FF regime, one is guaranteed that the constraints (25), (26), and (30) are satisfied. However, a potential disadvantage of such approach is also that there is no guarantee that the solution that is forced locally with the transformations (27)–(32) is compatible with the solutions in their neighborhoods and thus, that it leads to a smooth and accurate representation of the EM fields in the presence of current sheets.⁷ As we will show below, this concern is indeed well grounded, but it can be resolved effectively through the “driver” approach proposed here.

To compare the different FF prescriptions we have considered the simpler setup of a single spinning BH as this allows us to concentrate on stationary solutions and, hence, to isolate the potential drawbacks of the different prescriptions, which in a binary would otherwise be confused with the actual dynamics

of the EM fields. Figure 1 reports the time evolution of the 2-norms of the scalar product $E^i B_i$, i.e., $\|E^i B_i\|_2$ (left column) and of the fractional 2-norm of $(B^2 - E^2)$, i.e., $1 - \|B^2 - E^2\|_2 / (\|B^2 - E^2\|_2)_{t=0}$ (right column), monitoring possible deviations from the orthogonality condition of Equation (25) and from the current-sheet condition of Equation (30). The top row of Figure 1, in particular, refers to a single spinning BH, while the bottom row has been obtained in the case of the non-spinning BH binary system s_0 .

The different curves correspond to the various combinations in the specification of the current and in the treatment of the FF constraints. In particular, the labels in the legend of Figure 1 refer to the following choices:

1. **discrete₁**: denotes the first step of the “discrete” approach of Palenzuela et al. (2010a), which amounts to adopting Equation (26) with $J_B = 0$ for the current and to Equation (27) for ensuring the FF constraint (25).
2. **driver₁**: denotes the first step of our “driver” approach and which amounts to adopting Equation (26) with the parallel component of the current specified by Equation (29).
3. **discrete₂**: denotes the second step of the “discrete” approach of Palenzuela et al. (2010a), which amounts to the modification of the electric field according to Equation (32).
4. **driver₂**: denotes the second step of our “driver” approach and which amounts to adopting Equation (33) for the current.

⁷ Indeed, it is a common experience that any local numerical modification of the solution, e.g., in terms of boundary conditions, is likely to be incompatible with the solution in the bulk.

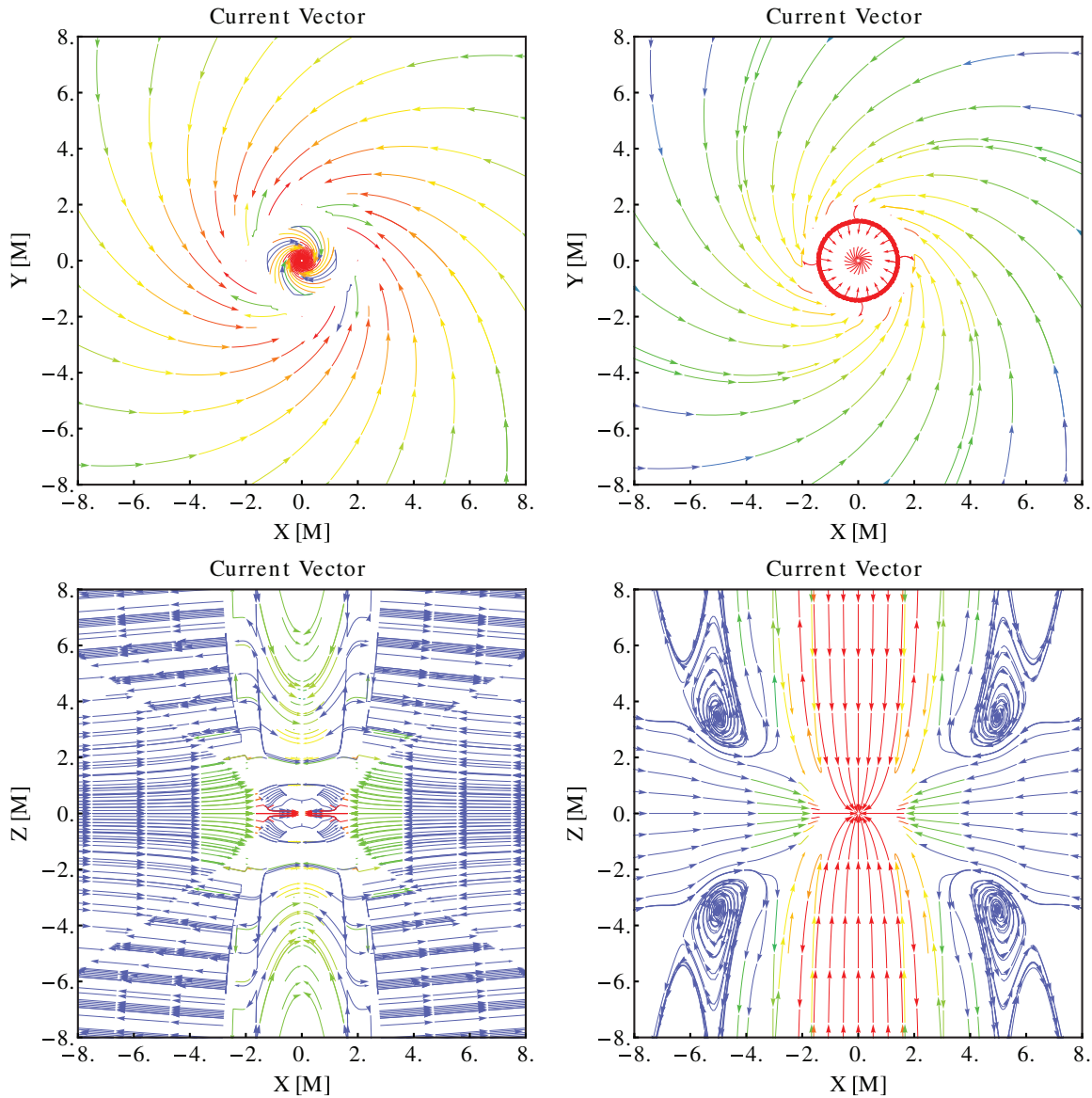


Figure 2. Comparison of the electric currents for a single spinning BH with dimensionless spin parameter $a = J/M^2 = 0.7$ on the plane $(x, y, z = 1.92 M)$ (top row) and on the plane $(x, y = 0, z)$ (bottom row). All panels refer to the same time $t = 102 M$, when the solution has reached a stationary state. The currents are computed either through the fully discrete approach of `discrete1`–`discrete2` (left column) or through our continuous `driver1`–`driver2` approach (right column). While both solutions satisfy the FF condition, it is clear that the use of the drivers provides also an accurate solution.

(A color version of this figure is available in the online journal.)

5. **continuum:** denotes the continuum approach in which the current is specified by Equation (31).

As it is evident from Figure 1, all of the methods satisfy the orthogonality condition (25) essentially to machine precision (left column). Not surprisingly, the discrete prescriptions `discrete1` (combined with `discrete2`) is particularly efficient in removing any component of the electric field parallel to B^i , either in isolated BHs (top row) or in the case of an inspiralling binary (bottom row). In this latter case, the bump of $E_i B^i$ at $t \sim 400 M$ simply corresponds to the time of the merger and the constraint decreases after that. Similarly, the right column of Figure 1 shows that all prescriptions are also able to enforce to comparable precision the current-sheet condition of Equation (30), but also that the discrete recipe (32) is slightly less effective in the case of an inspiralling binary (bottom right panel).

The main conclusion to draw from Figure 1 is that, at least globally, all methods provide a comparable and actually very good enforcement of the FF conditions. Their local performance, however, is rather different and this is shown in Figure 2, which reports the electrical currents as computed for a representative configuration of a single spinning BH with dimensionless spin $a = J/M^2 = 0.7$. In the top panels we have reported the current vectors in the plane $(x, y, z = 1.92 M)$, while in the bottom ones the currents in the plane $(x, y = 0, z)$. The two columns, on the other hand, contrast the currents when computed using the `discrete1` and `discrete2` approaches (left column) or when computed using our `driver1` and `driver2` approaches (right column).

A rapid comparison is sufficient to highlight that although both approaches yield an FF condition, the solution is very different, particularly on small scales. More specifically, when the combination of methods `driver1`–`driver2` is adopted (right

column), strong meridional currents are clearly visible and form a jet-like structure, with negative currents in the central parts of the jet and positive ones on the edges of the jet. This current distribution is what is expected and it resembles the typical structure of the FF magnetosphere of a rotating BH obtained through the solution of the Grad–Shafranov equation (see, for instance, Figure 7 in Beskin 1997). On the other hand, the corresponding currents when the prescriptions `discrete1` and `discrete2` are used (right column) do not show evident signs of descending currents and, rather, they show unphysical features around the BH and discontinuities along the $\sim \pm 45^\circ$ diagonals when seen in the (x, z) plane. In addition, the currents tend to be predominantly contained in planes which are parallel to the (x, y) plane (see the top row) and thus do not show the circulations which are instead captured with our drivers approach.

Overall, the comparison presented in Figure 2 confirms our suspicions that, while providing a solution that is globally FF, the prescriptions `discrete1` and `discrete2` are not guaranteed to yield solutions that are locally accurate and can actually lead to solutions with large discontinuities. For these reasons we believe that our approaches `driver1`–`driver2` should be preferred in treatments of FF electrodynamics. As a final remark we also note that our prescriptions (29) and (33) also provide a (small) saving in computational costs. Since we use an algebraic prescription for the current which automatically drives the solution to the FF regime, we do not need to perform the expensive checks at every gridpoint that come with the approach suggested in Palenzuela et al. (2010a).

6. FORCE-FREE ELECTRODYNAMICS OF BBH MERGERS

After having discussed the details of our implementation of the FF conditions and having shown its higher accuracy with respect to alternative suggestions in the literature, in the following we concentrate our discussion on the FF electrodynamics accompanying the inspiral and merger of BH binaries. In particular, we will discuss the subtleties that emerge with the subtraction of the background radiation, the spatial distribution of the charge density, the EM and GW zones, and the scaling of the EM luminosity with frequency.

6.1. Subtraction of Background Radiation

As anticipated in Section 3, our measure of EM radiation is influenced by the choice of a uniform initial magnetic field within the computational domain, which leads to nonzero initial values for Φ_2 and Φ_0 . Hence, a proper identification of this background radiation is essential for the correct measure of the emitted luminosity and to characterize its properties.

The generic expression (37) for the EM luminosity can be evaluated in combination with Equation (39), that is, by setting as background values those of the Newman–Penrose scalars Φ_2 and Φ_0 at the initial time. Note that initial values of these scalars are the same as they have in an electrovacuum scenario (they are indeed the same considered in Mösta et al. 2010), and thus the “background subtraction” corresponds in this case to the subtraction of the EM emission coming from a magnetic field which is asymptotically uniform. Of course, the initial time is as good as any other time and we could, in principle, choose $\Phi_{2,B}$ and $\Phi_{0,B}$ at any time $t > 0$. In this case, however, we would have to deal with the additional complication that for any choice other than $t = 0$, the background radiation will also have

an azimuthal modulation as a result of the orbital motion and hence it will not be simply an $m = 0$ background.

The angular distribution of the emitted radiation when projected onto a 2-sphere, in fact, shows the presence of two jets but also of two extended lobes, which rotate at the same frequency as the binary and that provide the bulk of the EM emission (see Figure 1 of Paper I). As a result, any background subtraction at $t \neq 0$ will also have an $m = 2$ component which will interfere with the $m = 2$ evolution of the emitted flux, introducing a modulation on the emission. The latter, however, will average over one orbit, leading to a net emitted luminosity which is the same obtained when using $\Phi_{2,B} = \Phi_2(t = 0)$ and $\Phi_{0,B} = \Phi_0(t = 0)$. We have verified that this is indeed the case by using background values at different times and obtained values of the luminosity which can be instantaneously different, but that once integrated over time yield the same emitted EM energy. As a result, the background choice (39) represents by far the most convenient one.

We have also mentioned in Section 3 that an alternative and equivalent estimate of the emitted EM luminosity can be obtained after removing the non-radiative parts of the emission (cf. expression (40)). In order to isolate the radiative contributions from the non-radiative ones, we have reported in Figure 3 the evolution of the real (thick lines) and of the imaginary (thin lines) parts of the $\ell = 2, m = 0$ and $\ell = 2, m = 2$ modes of Φ_2 and Φ_0 . These modes are obtained from the projection of the Faraday tensor onto the tetrad (35). Note that the only modes that have a regular time modulation, and are therefore radiative, are $(\Phi_2)_{22}$ and $(\Phi_0)_{22}$, while the real parts of the $(\Phi_2)_{20}$ and $(\Phi_0)_{20}$ are essentially constant in time, indicating that these are not radiative modes, and could represent a way to measure the background radiation. The imaginary parts of $(\Phi_2)_{20}$ and $(\Phi_0)_{20}$, on the other hand, do show a regular evolution in time and a ringdown, but their values are much smaller (i.e., two orders of magnitude or more) and do not play a significant role in estimating the total radiation.

As a result, we can write expression (40) explicitly as

$$\Phi_{2,B} \simeq \text{Re}(\Phi_2)_{20}, \quad \Phi_{0,B} \simeq \text{Re}(\Phi_0)_{20}, \quad (43)$$

and in doing so we obtain an estimate that is very similar to the results reported in Neilsen et al. (2011), where expression (38) was used.

As discussed in Section 3, the use of Equation (38) as an estimate of the emitted luminosity is subject to the validity of the assumption $\Phi_{2,B} \approx \Phi_{0,B}$, or after using Equation (43), of $\text{Re}(\Phi_2)_{20} \approx \text{Re}(\Phi_0)_{20}$. This condition is true only as a first rough approximation, as shown in the right panel of Figure 3, which reports the evolution of $\text{Re}(\Phi_2)_{20}$ (red dotted line) and of $\text{Re}(\Phi_0)_{20}$ (black dashed line), as extracted at $100M$ for the non-spinning binary s_0 . Clearly, these two multipoles are almost constant in time and comparable, but not identical, and their difference then affects the validity of expression (38). This consideration, together with the fact that expression (38) represents an approximation which needs to be validated a posteriori, leads us to the conclusion that Equation (37) represents a more accurate and robust measure of the emitted luminosity in the scenario and model considered here.

6.2. Properties of the EM Luminosity

Having clarified our strategy in the subtraction of the background radiation, we present in Figure 4 a comparison of the

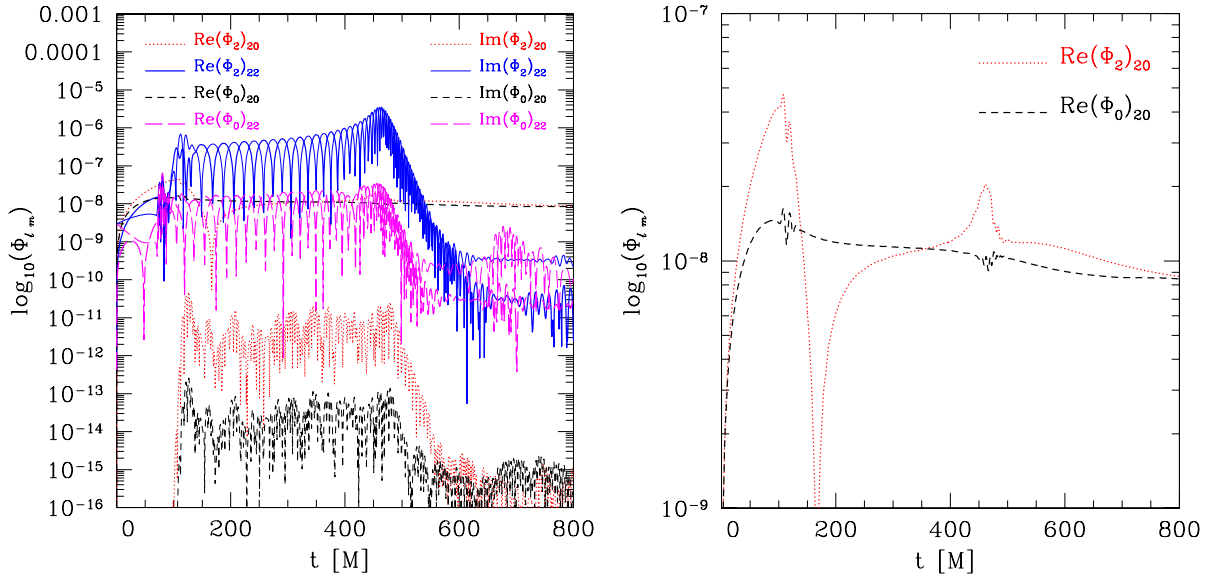


Figure 3. Left panel: evolution of the real (thick lines) and imaginary (thin lines) parts of the $\ell = 2, m = 0$ and $\ell = 2, m = 2$ modes of Φ_2 and Φ_0 , extracted at $100 M$ for the non-spinning binary s_0 . Right panel: the same as in the left panel but with a scale appropriate to highlight the evolution of $\text{Re}(\Phi_2)_{20}$ (red dotted line) and of $\text{Re}(\Phi_0)_{20}$ (black dashed line). Both are almost constant in time and comparable, but not identical.

(A color version of this figure is available in the online journal.)

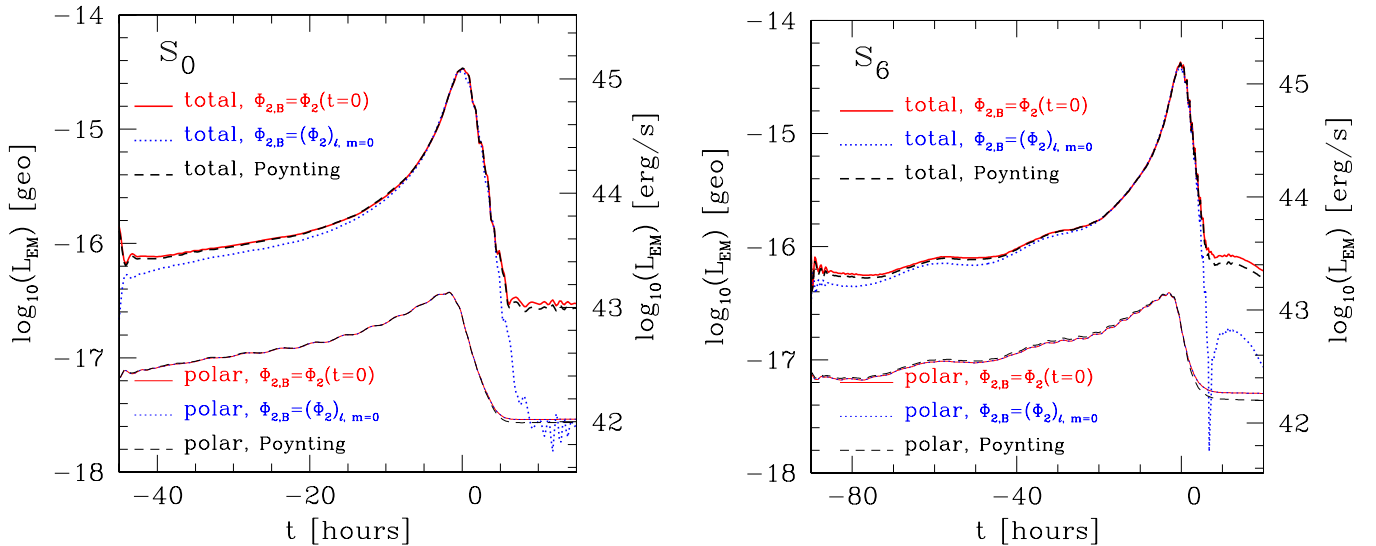


Figure 4. Time evolution measured in hours before the merger of the EM luminosity at $100 M$ when $M = 10^8 M_\odot$ and $B_0 = 10^4$ G. The thick lines refer to the total luminosity, while the thin ones to the luminosity in a polar cap of 5° semi-opening angle, measured using either expression (39) (red solid line), expression (40) (blue dotted line), or the flux using the Poynting vector in (41) (black dashed line). The left panel refers to the binary of non-spinning BHs (i.e., s_0), while the right one to the binary with spinning BHs (i.e., s_6). Note that in this latter case a certain eccentricity is detectable in the EM luminosity, although it is much smaller in the GW luminosity.

(A color version of this figure is available in the online journal.)

evolution, measured in hours before the merger, of the luminosities as computed with expression (37) and either the prescriptions (39) or (40) for the background subtraction.

More specifically, the thick lines refer to the total luminosity, while the thin ones to the luminosity in a polar cap of 5° semi-opening angle, measured using either expression (39) (red solid line), expression (40) (blue dotted line), or through the expression in terms of the Poynting vector (41) (black dashed line). The left panel refers to the binary of non-spinning BHs (i.e., s_0), while the right one to the binary with spinning BHs (i.e., s_6). In both cases the extraction is made at a distance of $100 M$ and the values in cgs units refer to a binary with a total $M = 10^8 M_\odot$ and a magnetic field $B_0 = 10^4$ G. Such

magnetic-field strengths match the values as estimated from radio observations of parsec-scale jets in active galactic nuclei (O'Sullivan & Gabuzda 2009).

As expected, the three measures match very well and, in particular, the measure made with expression (39) is remarkably close to the one obtained in terms of the Poynting vector (41), that we consider the most robust measure since it directly involves our primary evolution variables E^i and B^i . After the merger, both luminosities converge to a constant value which is larger than one coming from the polar-cap region (cf. thin lines). This is due to the fact that the background subtraction refers to a pure electrovacuum-condition (i.e., uniform magnetic field in a flat spacetime) and thus it does not provide an

accurate description of an isolated spinning BH. Subtracting as background that of a single BH in electrovacuum would bring the two curves down to the values of the polar cap, but we have not shown this in Figure 4 to avoid a cluttering of curves. Note also that the measure made with expression (40) is effectively subtracting the initial background emission and, at the same time, also including some incoming radiation (this is true also for the measures presented by Palenzuela et al. 2010a, 2010b). As a result, this measure is always (slightly) smaller than the one obtained with either prescriptions (39) or (41). For the same reason, the contributions coming from the dual jets will appear comparatively larger when using Equation (40).

Figure 4 also shows that the differences in the luminosities coming from the polar-cap region are instead much smaller and hardly noticeable. The reason behind this very good agreement is simple: being integrated over a small solid angle these luminosities are not influenced by the dissimilarities that the different prescriptions show instead in the emitted luminosity. Overall, Figure 4 shows that, as the merger takes place, both the diffused and the collimated EM luminosity increase steeply, reaching values at the merger that are about 50 times larger than the corresponding ones a few orbits before the merger. The growth in the diffused luminosity, however, is larger than the one in the collimated luminosity and the difference in the two, which was already present at the beginning of the simulations, increases as the inspiral proceeds. As a result, at the merger the non-collimated (total) emission is ~ 100 times larger than the collimated one, reaching values $L_{\text{EM}} \simeq 10^{45} \text{ erg s}^{-1}$ for a $10^8 M_{\odot}$ binary⁸.

A few comments should be reserved about the different spatial distributions of the EM fluxes that come with the different prescriptions for the subtraction of the background radiation and that are erased when computing the luminosities as integral quantities. First of all, we note that the EM flux in Equation (37) is not necessarily positive on the 2-sphere and that (small) negative contributions can appear (see Figure 1 of Paper I and the corresponding color bar). These emissions, however, do not represent a radiative field and average to zero over one orbit (this point was already remarked in Palenzuela et al. 2010c, where a toy model within the membrane paradigm was used for the binary). This non-radiative part is far from being uninteresting as it could lead to a different secondary emission as the EM fields interact with the plasma. Unfortunately, by construction, it is impossible to investigate such an emission within our FF approach, but this is clearly an aspect of this research that deserves further investigation. Second, as already remarked in Paper I, while the EM fluxes do contain a dual-jet structure and even if the fluxes at the jets are ~ 8 – 2 times larger than elsewhere, the global spatial distribution is effectively dominated by a non-collimated emission of quadrupolar nature, drastically changing the prospects of the detectability of the dual jets (see also discussion below). Finally, the local EM flux from the jets can, in principle, be enhanced if the BHs are spinning and, indeed, within a Blandford–Znajek process one expects that the luminosity from the jets increases quadratically with the spin of the BH (Blandford & Znajek 1977; Palenzuela et al. 2010b). The differences introduced by the spin are reported in the right panel of Figure 4, which refers to the binary s_6 and thus with BHs having a dimensionless spin of $J/M^2 \simeq 0.6$. Clearly, both the collimated and the non-collimated emission

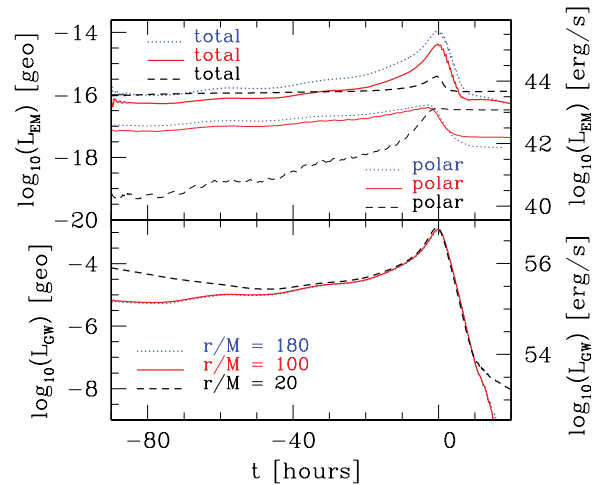


Figure 5. Evolution of the EM (top panel) and the GW luminosity (bottom panel) integrated over 2-spheres located, respectively, at $r = 20, 100$, and $180 M$. Thick lines refer to the diffused emission, while thin ones to the emission from a polar cap of 5° semi-opening angle; the data refer to the spinning s_6 binary and both the EM and the GW luminosities are computed including modes up to the $\ell = 8$ multipole. Note that the gravitational-wave zone is already well defined at $100 M$, while the EM one is not even at $180 M$.

(A color version of this figure is available in the online journal.)

show a behavior that is similar to the one seen for the s_0 binary, with only a 50% enhancement of the EM radiation, both in the total and in the collimated emission (note that the two panels in Figure 4 have the scale). This result is the consequence of the fact that most of the radiation that is produced is diffused and produced by the interaction between the BH orbital motion and the background magnetic field. Indeed, we find that the emission in the electrovacuum evolution as computed in Mösta et al. (2010) is comparable to the FF one (this is different from what reported in Palenzuela et al. 2010a, 2010b). The local spin enhancement in the dual jets is therefore present, but still much smaller than the diffused emission, which remains the predominant one at these separations.

It is always useful to remark that by construction the Newman–Penrose scalars, either for the gravitational sector, i.e., Ψ_4 , or for the EM one, i.e., Φ_0, Φ_2 , provide non-ambiguous quantities only at very large distances from the sources, that is, in the corresponding “wave zone.” It is obvious then that any measure of such radiation quantities in the strong-field region risks to be incorrect. Less obvious, however, is the fact that the wave zones can be different whether one is considering the gravitational or the EM radiation, with the latter starting at considerably larger distances than the former. This is summarized in Figure 5, which reports the EM (top panel) and the GW luminosity (bottom panel) integrated over 2-spheres located, respectively, at $r = 20, 100$, and $180 M$. The data refer to the spinning s_6 binary, with both the EM and the GW luminosities having been computed including modes up to the $\ell = 8$ multipole; thick lines refer to the diffused emission, while thin ones to the emission from a polar cap of 5° semi-opening angle. Clearly, the estimates made at $r = 20 M$ in both channels are rather different (and incorrect) from those made at larger radii, where the radiation has reached its wave-like solution. Also striking is that while the GW estimates at $100 M$ and $180 M$ are essentially indistinguishable (bottom panel), the corresponding ones in the EM channel are not yet identical. This indicates first that the GW zone is much closer than the EM one and reached already at $r \sim 100 M$, and, second, that

⁸ Note that the local flux of the collimated emission can be ~ 8 – 2 times larger than the one in the diffused emission. However, being limited to a very small solid angle, the corresponding luminosity is 100 times smaller.

extraction radii larger than $r \sim 200 M$ should be considered when measuring the EM radiation. We note that the evidence of a relative “proximity” of the GW zone to the strong-field dynamical region of spacetime is somewhat surprising, but also in substantial agreement with the bulk of evidence emerging in favor of a description of the dynamics of the BHs that is very well described by PN or other approximation techniques. This good agreement is indeed perfectly understandable if the weak-field wave zone starts only a few tens of M away from the BHs.

6.3. Frequency Scaling

As remarked already in Paper I, an accurate measure of the evolution of the collimated and non-collimated contributions of the emitted energies is crucial to predict the properties of the system when the two BHs are widely separated. This measure, however, is all but trivial as it requires a reliable disentanglement of the collimated emission from the non-collimated one and from the background. We have seen in Figure 4 how the total EM luminosities show a very similar evolution as long as sensible subtractions of the background radiation are used. We have also discussed that independently of the choice made, the diffused emission is mostly quadrupolar and hence with a dependence that is the same as the GW one, i.e., $\sim \Omega^{10/3}$, as already shown by Palenzuela et al. (2010c) and Mösta et al. (2010). Figure 6 considers more closely this issue by reporting in the left panel the change of the different gravitational and EM luminosities in the orbital evolution as a function of the GW frequency Ω_{GW} . More specifically, we report the diffused EM radiation as computed with expressions (37) and (40) (red solid line) and the collimated emission when computed over a polar cap with a semi-opening angle of 5° (blue solid line). Also shown is the evolution of the GW luminosity (black solid line) scaled down of a factor 10^{-10} to make it comparable with the other luminosities (we recall that the efficiency in GW emission is ~ 13 orders of magnitude larger as first shown in Mösta et al. 2010). The short-dashed, dotted, and long-dashed lines show instead the different scalings (note the figure is a log–log plot).

It is then straightforward to realize that at the separations considered here the diffused emission shows a scaling with frequency which is $L_{\text{EM}}^{\text{non-coll}} \approx \Omega^{10/3-8/3}$, thus compatible with the scaling shown by the GW emission. The collimated emission, however, has a slower growth, with a scaling that is $L_{\text{EM}}^{\text{coll}} \approx \Omega^{5/3-6/3}$. This is different from the predicted scaling of $L_{\text{EM}}^{\text{coll}} \approx \Omega^{2/3}$ suggested in Palenzuela et al. (2010b), and that we show with a light-blue long-dashed line. This difference is probably due to the fact that the estimate in Palenzuela et al. (2010b) was made by studying the behavior of boosted BHs and then extrapolating the result to the case of orbiting BHs. The scaling $\sim \Omega^{2/3}$ is clearly incompatible with our data and we suspect the accelerated motion of the BHs to be behind this difference and longer simulations will be useful to draw robust conclusions.

Given that the diffused and the collimated emissions scale differently with frequency and using the rough estimates made above for their scaling at earlier times,⁹ we can determine the frequency (or time) when the collimated emission will be dominant relative to the diffused one. This is shown in

the right panel of Figure 6, which is the same as the left one but where we extrapolate the scaling back in frequency. Our rough estimate is therefore that the collimated emission will be larger than the diffused one at an orbital frequency $\Omega = (1/2)\Omega_{\text{GW}} \simeq 3.2 \times 10^{-5} \text{ Hz}$ and thus $\simeq 21$ days before the merger. If the conditions are optimal and the binary is oriented in such a way that the dual-jet system points toward the Earth, the luminosity from the binary would therefore be modulated on timescales $\tau \lesssim 1/\Omega \simeq 8.6 \text{ hr}$ and smaller. While this is an exciting possibility, we should also bear in mind that, when extrapolated back to the time when it becomes dominant, the collimated emission has also decreased by almost one order of magnitude and to luminosities that are only of the order of $\sim 10^{42} \text{ erg s}^{-1}$. Luminosities $\sim 10^{45} \text{ erg s}^{-1}$ are also typical of radio-loud galaxies and thus the determination of an EM counterpart can be challenging if such sources are near the candidate event. Clearly, the bottom line of these considerations is that longer simulations need to be performed to assess the early inspiral scaling of the different luminosities and more realistic scenarios need to be considered to assess whether the collimated or the diffused emission can serve as an EM counterpart to the merger of binary system of supermassive BHs (see Giacomazzo et al. 2012 and Noble et al. 2012 for some recent attempts).

6.4. Charge-density Distribution

In this concluding section we concentrate on the spatial distribution of the charge density produced during the inspiral and merger, providing information which is complementary to the one already presented by Palenzuela et al. (2010b, 2010c) and Neilsen et al. (2011). We recall that in our simulations the charge density is not an evolutionary quantity, but, rather, it is computed from the constraint Equation (7). We also recall that because we are very effective in enforcing the FF condition (see discussion in Section 5), we cannot fully explore the physical consequences of the charge distribution we produce. This is because in the most interesting regions of these distributions, that is, in those regions with no (or very small) net charges and which are reminiscent of the vacuum-gap regions in pulsar magnetospheres (Becker 2009), the electric field along the magnetic field will be zero to machine precision and hence it will not be able to accelerate particles to very high Lorentz factors (as instead is expected in the polar regions of pulsar magnetospheres). To further limit the amount of information that can be extracted directly from our simulation is the fact that an FF code does not allow for an unambiguous calculation of the plasma velocity, which can only be estimated a posteriori based on a certain number of assumptions. As an example, Hirotani & Okamoto (1998) argued that it is possible to compute the final Lorentz factor of a plasma in an FF magnetosphere if there is a non-negligible component of the parallel electric field and a radiation drag dominated by Thompson scattering.

In spite of these limitations, the charge-density distribution remains a very interesting quantity and we have reported it in Figures 7 and 8. The three top panels of Figure 7, in particular, show the charge distribution on the (x, y) plane, while the bottom ones on the (x, z) planes at three different instants in the evolution of the spinning binary s_6 . More specifically, in the early inspiral phase ($t = 89 M$), at the merger ($t = 672 M$), and at ringdown ($t = 800 M$). The color code highlights the presence of positive (red) and negative (blue) charges, which are produced both because of the orbital motion of the BHs, but also because of the intrinsic spin of the BH. The first contribution can

⁹ In reality we expect the scaling with frequency to be different in the different stages of the inspiral, just as it is the case for the GW emission. However, as a first approximation we can assume that the frequency does not change significantly in the early stages of the inspiral.

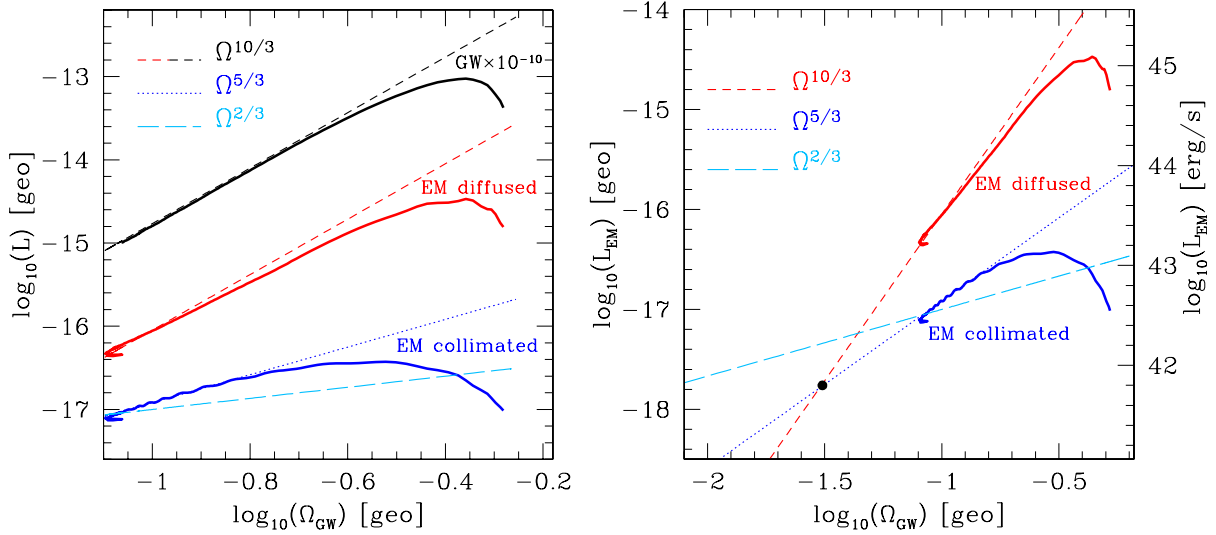


Figure 6. Left panel: frequency scaling for the non-spinning binary s_0 of the GW luminosity rescaled of a factor 10^{-10} (black solid line), of the diffused EM luminosity (red solid line), and of the collimated EM luminosity computed in a polar cap with a semi-opening angle of 5° (blue solid line). Note that the diffused EM luminosity has a behavior which is compatible with $\Omega^{10/3-8/3}$ as does as the GW luminosity. The collimated EM luminosity, on the other hand, has a scaling compatible with $\Omega^{5/3-6/3}$. Right panel: the same as in the left panel but reporting only the GW emission and extrapolating back in the past to determine when the collimated and the diffused emissions are comparable. For a binary with $10^8 M_\odot$ this happens ~ 21 days before merger.

(A color version of this figure is available in the online journal.)

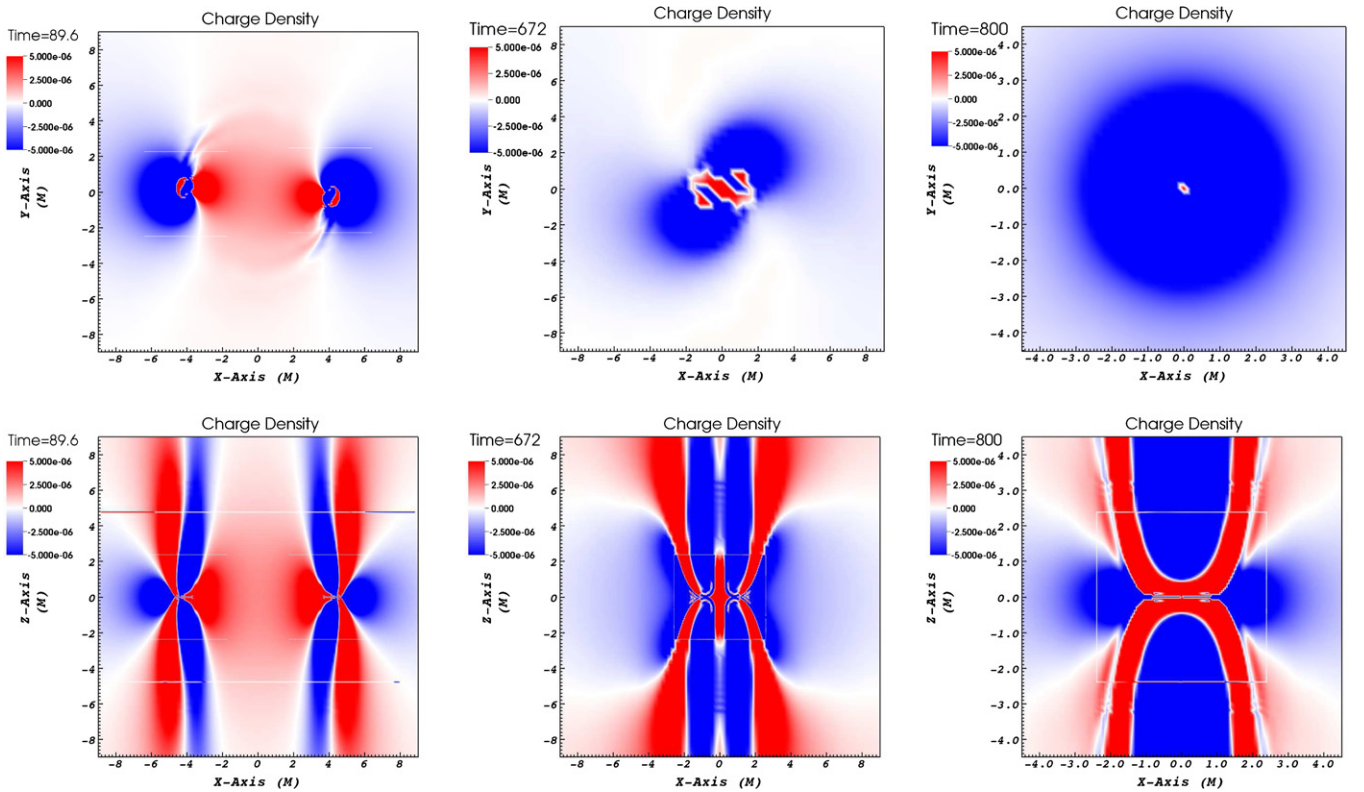


Figure 7. Small-scale two-dimensional distribution of the charge density for a s_6 binary in the early inspiral phase at $t = 89 M$ (left column), at merger $t = 672 M$ (middle column), and at ringdown $t = 800 M$ (right column). The top panels show the charge density in the (x, y) plane, while the bottom ones in the (x, z) plane. Visualizations artifacts appear as thin stripes at the boundaries between refinement levels; the data in those stripes are of course regular.

(A color version of this figure is available in the online journal.)

be appreciated from the first two columns of Figure 7, while the second contribution is the only one responsible for the charge distribution in the last column. Much of this distribution of charges can be easily interpreted within the membrane paradigm (Thorne et al. 1986) as the result of an effective Hall effect arising when the BH horizon (i.e., the “membrane”) moves,

either as a result the orbital motion or through its spinning motion, across a magnetic field. In analogy with the classical Hall effect, a charge separation will be produced as shown in Figure 7 (see also the discussion in Neilsen et al. 2011; Lyutikov 2011). Note that since they both refer to isolated spinning BHs (although with different spins), the right column of Figure 7

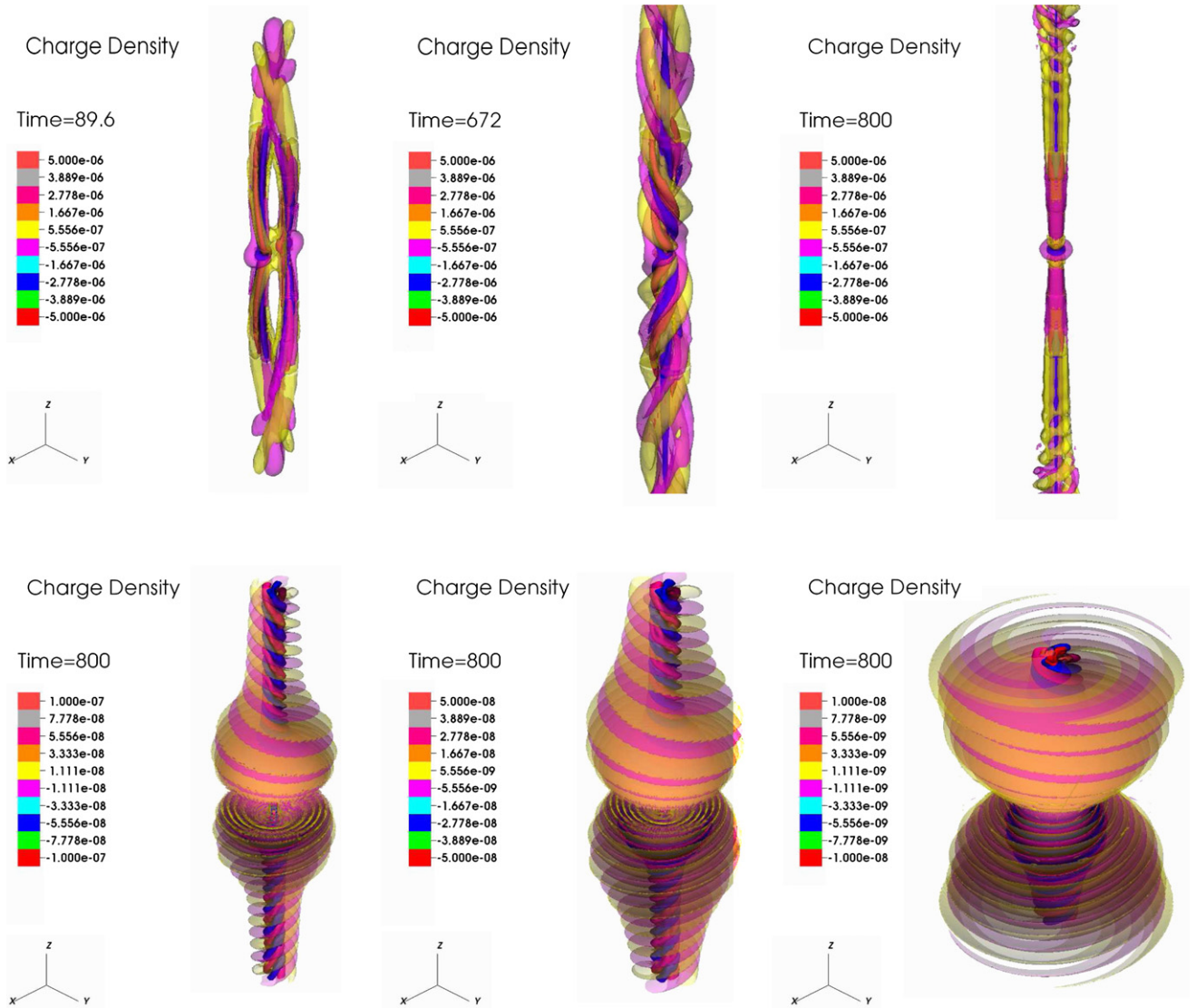


Figure 8. Top row: large-scale three-dimensional distribution of the charge density for the s_6 binary in the early inspiral phase at $t = 89 M$ (left panel), at the merger $t = 672 M$ (middle panel), and at ringdown $t = 800 M$ (right panel). In these panels only the largest values of the charge density are shown. Bottom row: three-dimensional distribution of the charge density at ringdown only, $t = 800 M$. Starting from the left, the panels show smaller and smaller values of the charge density, revealing a much more extended conical-shaped structure with a double-helical distribution of opposite charges. Clearly, charge-density distribution is far more complex than what would be deduced from the top panels only.

(A color version of this figure is available in the online journal.)

should be compared with the right column of Figure 2, which shows instead the electric currents.

Additional information is shown in Figure 8, where the charge-density distribution is rendered in three dimensions at the same representative times shown in the panels of Figure 7 and on much larger length scales. This representation highlights that the distribution is far more complex than a simple dual-jet structure and is instead typical of a double-helical symmetry, similar to the pattern for the Poynting flux shown in Palenzuela et al. (2010a, 2010b). Although it is not possible to investigate further, within an FF approach, the consequences of this regular and alternate distribution of positive and negative charges, it is clear that it can lead to rather intriguing particle acceleration processes along the surfaces separating regions of different charges. The resulting accelerated particles could further cascade into less energetic charges and lead to a potentially detectable emission.

It is worth remarking, however, that the charge-density distribution is not restricted to a small cylindrical area comprising

the two inspiralling BHs, as it may erroneously appear from the top panels of Figure 8, and which shows only the regions where the charge density is the largest. Rather, it involves the whole region in causal contact with the binary, as shown in the lower panels of Figure 8, which refer instead to the ringdown phase only ($t = 800 M$). Starting from the left, the different panels are drawn exhibiting increasingly smaller values of the charge density and thus revealing a much more extended conical-shaped structure with a double-helical distribution of opposite charges at its core. Additional investigations away from the FF regime will be necessary to assess the astrophysical impact of these structures.

7. PROSPECTS AND CONCLUSIONS

Assessing the detectability of the EM emission from merging BH binaries is much more than an academic exercise. The detection of EM counterpart, in fact, will not only act as a confirmation of the GW detection, but it will also provide a

new tool for testing a number of fundamental astrophysical issues (Haiman et al. 2009). In particular, it will offer the possibility of testing models of galaxy mergers and accretion disks, of probing basic aspects of gravitational physics, and of determining cosmological parameters once the redshift is known (Phinney 2009).

Computing reliable estimates from this scenario is made difficult by the scarce knowledge of the physical conditions in the vicinity of the binary when this is about to merge. Nevertheless, relying on a number of assumptions with varying degree of realism, several investigations have been recently carried out to investigate the properties of these EM counterparts either during the stages that precede the merger or in those following it. As an example, several authors have recently considered the interaction between the binary and a dense gas cloud (Armitage & Natarajan 2002; van Meter et al. 2010; Bode et al. 2010, 2012; Farris et al. 2010, 2011; Lodato et al. 2009; Chang et al. 2010; Giacomazzo et al. 2012; Noble et al. 2012) even though astrophysical considerations seem to suggest that during the very final stages of the merger the SMBBH will inspiral in a rather tenuous intergalactic medium. At the same time, scenarios that do not involve dense matter distributions in the vicinity of the binary have also been considered. In these cases, the SMBBH is assumed to be inspiralling in electrovacuum and in the presence of an external magnetic field which is anchored to the circumbinary disk (Palenzuela et al. 2009a; Mösta et al. 2010) and the energy emitted in EM waves is ~ 13 orders of magnitude smaller than the one emitted in GW for a typical binary of supermassive BHs with mass $M = 10^8 M_\odot$ in an ambient magnetic field of 10^4 G (Mösta et al. 2010).

Furthermore, when charges and currents are considered within an FF regime, the numerical results of Palenzuela et al. (2010a, 2010b) have shown that, if taking place in a uniform magnetic field, the merger event would be accompanied by the EM emission from a dual-jet structure, acting as a fingerprint of the merger itself. A detailed analysis carried out in Kaplan et al. (2011) addressed the problem of whether such merger flares can be detected by ongoing and planned wide-field radio surveys, such as the Square Kilometer Array pathfinder (Johnston et al. 2007). The conclusion was that, owing to the short timescales associated with the merger, no more than one event per year would be detectable by such blind surveys. In Paper I we have revisited the estimates made in Palenzuela et al. (2010a, 2010b) and shown that while a dual-jet structure is present during the inspiral, and while the fluxes can be larger near the jet, the collimated luminosity is subdominant of a factor ~ 100 with respect to the total luminosity, which is instead predominantly quadrupolar. Furthermore, spin-related enhancements are only very small and less than 50% when considering a spinning binary with dimensionless spins $J/M^2 = 0.6$.

Our results have been obtained adopting a consistent measurement of the EM luminosity and an improved numerical strategy for the treatment of the FF condition, both of which have been discussed in detail in this paper. More specifically, we have shown that we do not implement the FF condition at a discrete level, but rather we obtain it via a damping scheme that drives the solution to satisfy the correct condition. This difference is important for a correct and accurate description of the current sheets that can develop in the course of the simulation. We have also studied in greater detail the three-dimensional charge distribution produced as a consequence of the inspiral and shown that it possesses a complex but ordered structure with a double-

helical distribution of opposite charges tracing the motion of the two BHs.

Although our simulations show that the dual-jet structure is subdominant on the timescale over which the simulations have been carried out, they also indicate that the growth rates of the collimated and diffused luminosities are different, thus suggesting that sufficiently early in the inspiral the collimated emission will be the dominant one. Computing accurately these scaling rates is of course crucial since it allows for the determination of the time during the inspiral in which the dual jets are dominant and could modulate the emission if the binary is suitably oriented. When considering the observational implications of this possibility, O’Shaughnessy et al. (2011) have concluded that future blind radio surveys like VAST (Banyer et al. 2012) would easily detect the effects of these modulations, with a frequency of up to one per day.

We have therefore provided the first quantitative estimates of the scaling of the EM emission with frequency and shown that the diffused part has a dependence that is very close to the one exhibited by the GW luminosity and therefore of the type $L_{\text{EM}}^{\text{non-coll}} \approx \Omega^{10/3-8/3}$. The collimated EM emission, on the other hand, scales like $L_{\text{EM}}^{\text{coll}} \approx \Omega^{5/3-6/3}$, thus with a steeper dependence than $L_{\text{EM}}^{\text{coll}} \approx \Omega^{2/3}$, as previously suggested by Palenzuela et al. (2010b). In light of these scalings and considering a non-spinning binary, we conclude that the collimated emission will be larger than the diffused one at an orbital frequency of $\simeq 3.2 \times 10^{-5}$ Hz and thus $\simeq 21$ days before the merger.¹⁰ When this happens, the collimated luminosity will be about an order of magnitude smaller than the one considered here and of the order of $\sim 10^{42}$ erg s⁻¹ for a typical $10^8 M_\odot$ binary in a magnetic field of 10^4 G. Such a luminosity is about 1000 times smaller than the typical luminosity of radio-loud galaxies and thus the determination of an EM counterpart can be challenging if such sources are near the candidate event.

As a concluding remark we note that while our study addresses several points that were not fully investigated before, it also leaves open a number of questions. One of these questions is the efficiency of the secondary emission that could be generated either by the diffused component or by the collimated one. The richly complex structure of the charge-density distribution, in fact, can be the site where even small electric fields along the magnetic field lines would be able to accelerate particles to very high Lorentz factors, leading to a secondary emission similar to the one expected in the polar regions of pulsar magnetospheres. Unfortunately, however, our use of an FF condition (and our ability to maintain it essentially to machine precision) prevents us from producing such electric fields and hence the corresponding accelerations. Another and related unresolved issue is the fate of the Poynting flux once it impacts the intergalactic medium. Even in the optimistic case in which the majority of the Poynting flux is converted into radio emission via synchrotron processes, the EM radiation (either collimated or diffused) will eventually exit the evacuated central region around the binary and penetrate in the ambient medium. When this happens, part of the Poynting flux will be converted into kinetic energy and reprocessed in several EM wavebands, not necessarily in the radio range.¹¹ Clearly, longer simulations

¹⁰ Clearly, this equivalence in the emission will take place much earlier (and at smaller luminosities) if the scaling is less steep than $\sim \Omega^{10/3}$.

¹¹ Numerical MHD simulations in the context of jets from active galactic nuclei suggest that in these cases more than 70% of the Poynting flux can be converted into kinetic energy leading to flows with Lorentz factors of the order of $\Gamma \sim 10$ (Komissarov et al. 2007).

Table 1
Explicit IMEX-SSP3(4,3,3) L-stable Scheme

0	0	0	0	0
0	0	0	0	0
1	0	1	0	0
1/2	0	1/4	1/4	0
	0	1/6	1/6	2/3

and more realistic scenarios are needed to shed further light on the properties of the EM counterpart to the inspiral and merger of binary of supermassive BHs.

We thank L. Lehner and C. Palenzuela for insightful discussions on the analysis of the radiated quantities. We are grateful to E. Schnetter for his help in the implementation of the RKIMEX methods, I. Hinder and B. Wardell for some of the analysis tools used in this work, and E. Bentivegna and K. Dionysopoulou for help with the visualization of the currents and charges. This work was supported in part by the DFG grant SFB/Transregio 7; the computations were made at the AEI and on the TERAGRID network (TG-MCA02N014).

APPENDIX

ON THE IMPLEMENTATION OF THE IMEX SCHEME

The prototype of the stiff system of partial differential equations can be written as

$$\partial_t \mathbf{U} = \mathbf{F}(\mathbf{U}) + \sigma \mathbf{R}(\mathbf{U}), \quad (\text{A1})$$

where $1/\sigma > 0$ is the relaxation time. In the limit $\sigma \rightarrow \infty$ the system becomes stiff, since the relaxation of the stiff term $\mathbf{R}(\mathbf{U})$ is very different from the timescale of the non-stiff part $\mathbf{F}(\mathbf{U})$.

The evolution of the electric field (17) becomes stiff for high values of the conductivity σ_B in the Ohm law (26). We perform a split of its right-hand side in potentially stiff terms and regular ones,

$$\partial_t \mathbf{E} = \mathbf{F}_E + \mathbf{R}_E, \quad (\text{A2})$$

where

$$\begin{aligned} \mathbf{F}_E = & \epsilon^{ijk} e^{4\phi} [(\partial_j \alpha) \tilde{\gamma}_{ck} B^c + \alpha (4 \tilde{\gamma}_{ck} \partial_j \phi + \partial_j \tilde{\gamma}_{ck}) B^c \\ & + \alpha \tilde{\gamma}_{ck} \partial_j B^c] + \mathcal{L}_\beta E^i - \alpha K E^i - \alpha q \frac{\epsilon^{ijk} E_j B_k}{B^2}, \\ \mathbf{R}_E = & -\alpha J_B \frac{B^i}{B^2}. \end{aligned} \quad (\text{A3})$$

A solution for the magnetic field is obtained by evolving Equation (18) using only the explicit part of the Runge–Kutta solver. The evolution of the electric field uses both the explicit part of the Runge–Kutta solver (see Table 1) for the \mathbf{F}_E and the implicit part for \mathbf{R}_E (see Table 2), and leads to an approximate solution $\{\mathbf{E}_*\}$. The full solution requires inverting the implicit equation

$$\mathbf{E} = \mathbf{E}_* + a_{ii} \Delta t \mathbf{R}_E(\mathbf{E}), \quad (\text{A4})$$

which depends on the fields $\{\mathbf{B}, \mathbf{E}_*\}$.

In the case of the Ohm law (29) the stiff part is linear in \mathbf{E} , so an analytic inversion can be performed

$$\mathbf{E}^i = (\mathbf{M}_k^i)^{-1} \mathbf{E}_*^k, \quad (\text{A5})$$

Table 2
Implicit IMEX-SSP3(4,3,3) L-stable Scheme

α	α	0	0	0
0	$-\alpha$	α	0	0
1	0	$1 - \alpha$	α	0
1/2	β	η	$1/2 - \beta - \eta - \alpha$	α
	0	1/6	1/6	2/3

$$\mathbf{M}_k^i = \delta_k^i + a_{ii} \Delta t \alpha \sigma_B B_k \frac{B^i}{B^2}. \quad (\text{A6})$$

However, in the case of the Ohm law (33), the inversion is more involved as the stiff part is not linear in \mathbf{E} . We use the following simplified inversion:

$$\begin{aligned} \mathbf{E}^i = & (\mathbf{M}_k^i)^{-1} \mathbf{E}_*^k, \\ \mathbf{M}_k^i = & \delta_k^i + a_{ii} \Delta t \alpha \sigma_B \left(B_k \frac{B^i}{B^2} + \delta_k^i (E_*^2 - B^2) \frac{E_*^i}{B^2} \right). \end{aligned} \quad (\text{A7})$$

In the above equations, Δt is the timestep and a_{ii} are the diagonal coefficients of the implicit part of the RKIMEX matrix, whose tableau for the explicit and explicit-implicit IMEX-SSP3(4,3,3) L-stable scheme are reported below, where

$$\begin{aligned} \alpha = & 0.24169426078821, \beta = 0.06042356519705, \\ \eta = & 0.12915286960590. \end{aligned}$$

REFERENCES

- Allen, G., Goodale, T., Lanfermann, G., Radke, T., & Seidel, E. 2000, Proceedings of First Egrid Meeting at ISTHMUS, Poznan, <http://www.zib.de/visual/projects/TIKSL/Papers/EGrid2000-Cactus.ps>
- Amaro-Seoane, P., Aoudia, S., Babak, S., et al. 2012, arXiv:1201.3621
- Ansorg, M., Brüggemann, B., & Tichy, W. 2004, *Phys. Rev. D*, **70**, 064011
- Armitage, P. J., & Natarajan, P. 2002, *ApJ*, **567**, L9
- Baiotti, L., Giacomazzo, B., & Rezzolla, L. 2008, *Phys. Rev. D*, **78**, 084033
- Banyer, J., Murphy, T., & the VAST Collaboration. 2012, arXiv:1201.3130
- Barausse, E. 2012, MNRAS, 3050
- Becker, W. (ed.) 2009, Astrophysics and Space Science Library, Neutron Stars and Pulsars (Astrophysics and Space Science Library, Vol. 357; Berlin: Springer)
- Beskin, V. S. 1997, Sov. Phys. Usp., **40**, 659
- Binétruy, P., Bohé, A., Caprini, C., & Dufaux, J.-F. 2012, arXiv:1201.0983
- Blandford, R. D., & Znajek, R. L. 1977, MNRAS, **179**, 433
- Bode, T., Bogdanović, T., Haas, R., et al. 2012, *ApJ*, **744**, 45
- Bode, T., Haas, R., Bogdanovic, T., Laguna, P., & Shoemaker, D. 2010, *ApJ*, **715**, 1117
- Chang, P., Strubbe, L. E., Menou, K., & Quataert, E. 2010, MNRAS, **407**, 2007
- Cornish, N. J., & Porter, E. K. 2007, *Class. Quantum Grav.*, **24**, 5729
- Dedner, A., Kemm, F., Kröner, D., et al. 2002, *J. Comput. Phys.*, **175**, 645
- Dotti, M., Montuori, C., Decarli, R., et al. 2009, MNRAS, **398**, L73
- Ellison, S. L., Patton, D. R., Mendel, J. T., & Scudder, J. M. 2011, MNRAS, **418**, 2043
- Farris, B. D., Liu, Y. T., & Shapiro, S. L. 2010, *Phys. Rev. D*, **81**, 084008
- Farris, B. D., Liu, Y. T., & Shapiro, S. L. 2011, *Phys. Rev. D*, **84**, 024024
- Giacomazzo, B., Baker, J. G., Miller, M. C., Reynolds, C. S., & van Meter, J. R. 2012, *ApJ*, **752**, L15
- Gopal-Krishna, Biermann, P. L., & Wiita, P. J. 2003, *ApJ*, **594**, L103
- Haiman, Z., Kocsis, B., Menou, K., Lippai, Z., & Frei, Z. 2009, *Class. Quantum Grav.*, **26**, 094032
- Hirokani, K., & Okamoto, I. 1998, *ApJ*, **497**, 563
- Husa, S., Hannam, M., Gonzalez, J. A., Sperhake, U., & Bruegmann, B. 2008, *Phys. Rev. D*, **77**, 044037
- Johnston, S., Bailes, M., Bartel, N., et al. 2007, PASA, **24**, 174
- Kaplan, D. L., O’Shaughnessy, R., Sesana, A., & Volonteri, M. 2011, *ApJ*, **734**, L37

- Kesden, M., Lockhart, G., & Phinney, E. S. 2010, *Phys. Rev. D*, **82**, 124045
- Kocsis, B., Yunes, N., & Loeb, A. 2011, *Phys. Rev. D*, **84**, 024032
- Komissarov, S. S. 2004, *MNRAS*, **350**, 427
- Komissarov, S. S. 2006, *MNRAS*, **367**, 19
- Komissarov, S. S. 2007, *MNRAS*, **382**, 995
- Komissarov, S. S. 2011, *MNRAS*, **418**, L94
- Komissarov, S. S., & Barkov, M. V. 2009, *MNRAS*, **397**, 1153
- Komissarov, S. S., Barkov, M. V., Vlahakis, N., & Königl, A. 2007, *MNRAS*, **380**, 51
- Komossa, S., Burwitz, V., Hasinger, G., et al. 2003, *ApJ*, **582**, L15
- Koppitz, M., Pollney, D., Reisswig, C., et al. 2007, *Phys. Rev. Lett.*, **99**, 041102
- Lambas, D. G., Alonso, S., Mesa, V., & O'Mill, A. L. 2012, *A&A*, **539**, A45
- Liu, F., Wu, X., & Cao, S. 2003, *MNRAS*, **340**, 411
- Lodato, G., Nayakshin, S., King, A. R., & Pringle, J. E. 2009, *MNRAS*, **398**, 1392
- Lou, Y.-Q., & Jiang, Y.-F. 2008, *MNRAS*, **391**, L44
- Lyutikov, M. 2011, *Phys. Rev. D*, **83**, 064001
- MacFadyen, A. I., & Milosavljević, M. 2008, *ApJ*, **672**, 83
- Milosavljević, M., & Phinney, E. S. 2005, *ApJ*, **622**, L93
- Moesta, P., Alic, D., Rezzolla, L., Zanotti, O., & Palenzuela, C. 2012, *ApJ*, **749**, L32
- Mohamed, Y. H., & Reshetnikov, V. P. 2011, *Astrophysics*, **54**, 155
- Mösta, P., Palenzuela, C., Rezzolla, L., et al. 2010, *Phys. Rev. D*, **81**, 064017
- Neilsen, D., Lehner, L., Palenzuela, C., et al. 2011, *Proc. Natl. Acad. Sci.*, **108**, 12641
- Noble, S. C., Mundim, B. C., Nakano, H., et al. 2012, arXiv:1204.1073
- O'Shaughnessy, R., Kaplan, D. L., Sesana, A., & Kamble, A. 2011, *ApJ*, **743**, 136
- O'Sullivan, S. P., & Gabuzda, D. C. 2009, *MNRAS*, **400**, 26
- Palenzuela, C., Anderson, M., Lehner, L., Liebling, S. L., & Neilsen, D. 2009a, *Phys. Rev. Lett.*, **103**, 081101
- Palenzuela, C., Garrett, T., Lehner, L., & Liebling, S. L. 2010a, *Phys. Rev. D*, **82**, 044045
- Palenzuela, C., Lehner, L., & Liebling, S. L. 2010b, *Science*, **329**, 927
- Palenzuela, C., Lehner, L., Reula, O., & Rezzolla, L. 2009b, *MNRAS*, **394**, 1727
- Palenzuela, C., Lehner, L., & Yoshida, S. 2010c, *Phys. Rev. D*, **81**, 084007
- Phinney, E. S. 2009, *Astronomy*, **2010**, 235
- Pollney, D., Reisswig, C., Dorband, N., Schnetter, E., & Diener, P. 2009, *Phys. Rev. D*, **80**, 121502
- Pollney, D., Reisswig, C., Rezzolla, L., et al. 2007, *Phys. Rev. D*, **76**, 124002
- Pollney, D., Reisswig, C., Schnetter, E., Dorband, N., & Diener, P. 2011, *Phys. Rev. D*, **83**, 044045
- Reisswig, C., Husa, S., Rezzolla, L., et al. 2009, *Phys. Rev. D*, **80**, 124026
- Rezzolla, L. 2009, *Class. Quantum Grav.*, **26**, 094023
- Rezzolla, L., Barausse, E., Dorband, E. N., et al. 2008a, *Phys. Rev. D*, **78**, 044002
- Rezzolla, L., Diener, P., Dorband, E. N., et al. 2008b, *ApJ*, **674**, L29
- Rezzolla, L., Dorband, E. N., Reisswig, C., et al. 2008c, *ApJ*, **679**, 1422
- Rodriguez, C., Taylor, G. B., Zavala, R. T., et al. 2006, *ApJ*, **646**, 49
- Roedig, C., Dotti, M., Sesana, A., Cuadra, J., & Colpi, M. 2011, *MNRAS*, **415**, 3033
- Ruiz, M., Palenzuela, C., Galeazzi, F., & Bona, C. 2012, *MNRAS*, **2851**
- Schnetter, E., Hawley, S. H., & Hawke, I. 2004, *Class. Quantum Grav.*, **21**, 1465
- Sesana, A., Roedig, C., Reynolds, M. T., & Dotti, M. 2012, *MNRAS*, **420**, 860
- Shankar, F., Salucci, P., Granato, G. L., De Zotti, G., & Danese, L. 2004, *MNRAS*, **354**, 1020
- Tanaka, T., Menou, K., & Haiman, Z. 2012, *MNRAS*, **420**, 705
- Teukolsky, S. A. 1973, *ApJ*, **185**, 635
- Thorne, K. S., Price, R. H., & Macdonald, D. A. (ed.) 1986, *Black Holes: The Membrane Paradigm* (New Haven, CT: Yale Univ. Press)
- van Meter, J. R., Wise, J. H., Miller, M. C., et al. 2010, *ApJ*, **711**, L89